Powder Technology 424 (2023) 118539

Contents lists available at ScienceDirect

Powder Technology

journal homepage: www.journals.elsevier.com/powder-technology

Pyrolysis and CO_2 gasification of barley straw: Effect of particle size distribution and chemical composition

Antonia Gil *, Javier Pallarés, Inmaculada Arauzo, Cristóbal Cortés

Universidad de Zaragoza, IUI mixto CIRCE, Campus Rio Ebro, Mariano Esquillor Gómez, 15, 50018 Zaragoza, Spain

HIGHLIGHTS

- A wide size distribution and heterogeneity of barley straw after milling is observed.
- Inorganic content is significantly increased as the particle size is reduced.
- High Si content is detected in SEM-EDX images of particles coming from barley leaves.
- Char gasification rate is higher for the finest fraction below 750 °C by catalytic effects.
- Char gasification rate decreases at T >750°C for particle sizes <0.15 mm by the Si/K influence.

GRAPHICAL ABSTRACT

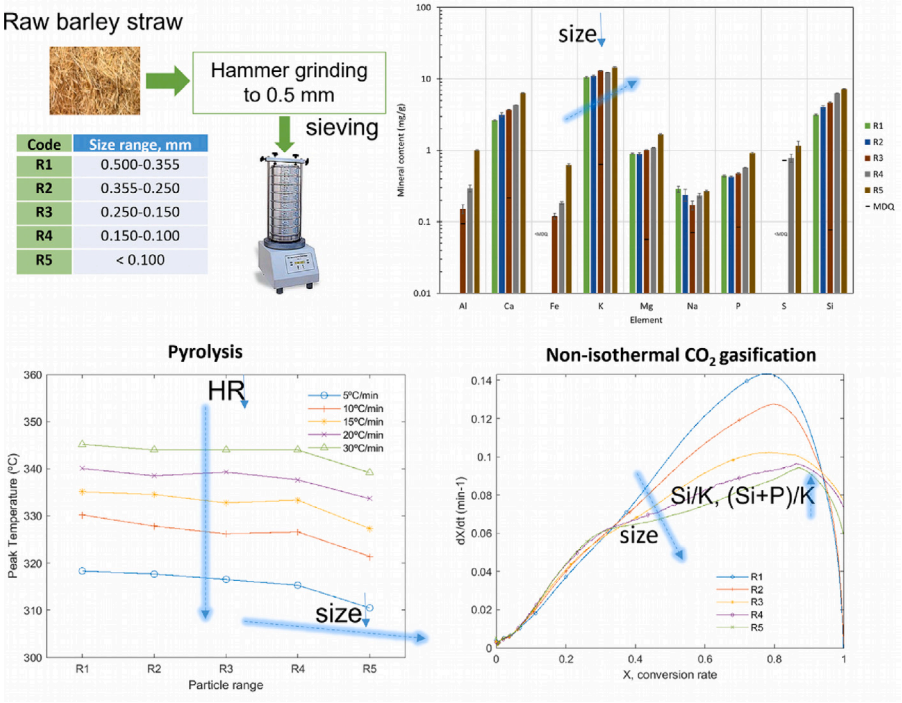

ARTICLE INFO

Keywords:
Activated carbon
Barley straw
Pyrolysis
CO_2 gasification
Particle size
Silicon content

ABSTRACT

We evaluate how the heterogeneity of the precursor may affect pyrolysis and CO_2 gasification behavior aimed at activated carbon applications. Barley straw, ground and classified into five size ranges, is characterized by non-isothermal thermogravimetry tests at various heating rates. Fixed carbon and volatile matter contents decrease with particle size. Also, the finest fraction is enriched in minerals by exogenous contamination and accumulation of silicon-rich leaves. Faster pyrolysis kinetics are found for small sizes, caused by their higher alkali contents and heat-mass transfer rates. Char-CO_2 gasification conversion rates show an unexpected behavior, not previously reported. Higher reactivity is found for the finest fraction, decreasing significantly at temperatures beyond 750 °C. The high alkali content of the finest fraction promotes the catalytic effect

* Corresponding author.
E-mail address: antgilma@unizar.es (A. Gil).

https://doi.org/10.1016/j.powtec.2023.118539
Received 10 December 2022; Received in revised form 22 February 2023; Accepted 8 April 2023
Available online 14 April 2023

of minerals on gasification reactivity at lower temperatures, hindering the reaction at higher temperatures by forming low-melting-point potassium silicates. Results help improve pretreatment strategies to enhance activated carbon quality.

Nomenclature

Abbreviations

$AAEM$	Alkaline and Alkaline Earth Metal
EDX	Energy Dispersive X-ray
FC	Fixed Carbon
$FE-SEM$	Field Emission Scanning Electron Microscope
HR	Heating Rate
$ICP-OES$	Inductively Coupled Plasma-Optical Emission Spectrometry
$JCPDS$	Joint Committee on Powder Diffraction Standards
M	Moisture
MDQ	Minimum Detectable Quantity
S	Gasification characteristic index
T_f	Final gasification temperature
T_i	Initial gasification temperature
t_R	Gasification time
TGA	ThermoGravimetric Analysis
VM	Volatile Matter
XRD	X-ray Diffraction

1. Introduction

Biomass-derived activated carbon has attracted a growing interest in recent years due to its excellent characteristics as a precursor, availability, and low cost. Straw is a promising biomass feedstock for environmental-friendly energy applications since large quantities are produced worldwide. There are numerous applications of activated biochar with good prospects for the future: energy storage, electrochemistry, wastewater treatment, and catalyst support, among others [1–9]. However, each application needs special treatment and tailored production conditions. To obtain activated biochar, chemical and physical routes are usually applied. During chemical activation, raw materials are firstly treated with activating agents such as H_3PO_4, $ZnCl_2$, and KOH, and then heated in an inert atmosphere. Although chemical activation is a widely accepted treatment, using chemicals may lead to secondary environmental pollution and equipment corrosion. Physical activation, however, is frequently used at the industrial scale due to its simplicity. This technique firstly involves the thermal treatment of raw materials (400–600 °C) under an inert atmosphere (usually nitrogen). Subsequently, heat treatment under the oxidizing gas (usually steam and/or CO_2) is applied within an activation temperature range of 800 to 1000 °C. Generally, the use of carbon dioxide is preferred due to its lower reactivity at high temperatures, which makes the activation process easier to control.

Despite their advantages, the inherent physicochemical heterogeneity of biomass residues may considerably alter the surface texture and pore development during the activation process, affecting their final quality [2]. It is well known that alkaline and alkaline-earth metals (AAEM) act as catalysts for the gasification reaction [10]. In contrast, Si and Al are inhibitors [11,12], causing agglomeration at high temperatures [13]. If there is a high Si concentration in biomass, Si reacts with K to form silicates, blocking the catalytic effect of K [14]. It has been observed that the reactivity of biochar in CO_2 gasification depends on the K/Si ratio [15]. The molar ratio (Si+P+K)/(Ca+Mg) has often been used as a global indicator to predict tendencies to form low ash melting points when this ratio is increased [13]. In addition, the alkali index (AI), defined as the ratio of the sum of the mass fraction of alkali compounds (Fe_2O_3+CaO+MgO+Na_2O+K_2O) to the sum of the mass fraction of acid compounds (SiO_2+Al_2O_3) detected in ashed samples, multiplied by the ash content of the biomass, has also been related to the gasification reactivity of the char. Several authors have identified AI as a qualitative measure to predict the reactivity of the gasification process for various coals [12,16,17] and biomass [13,15,18–20], finding that the increase of the alkali index enhances char gasification reactivity. Still, extensive research is mainly focused on the char properties after pyrolysis rather than on the raw material itself.

Regarding particle size distribution, although wood and coal pyrolysis characteristics have been extensively studied in the last decades, research works dealing with the effect of particle size on straw pyrolysis and gasification are less numerous, and the differences in chemical composition with particle size are scarcely reported. Table 1 summarizes relevant references. Although previous research on the miscanthus pyrolysis of 0.12 mm-and-1 mm size concluded that an 8-fold difference in the level of grinding did not result in substantial differences in the thermal decomposition [21], the opposite was observed when studying the thermal characteristics of two energy crops (reed canary grass and switchgrass), classified into two different size fractions (<0.09 mm and 0.09–0.6 mm) [22]. The authors found that smaller particles had a higher inorganic matter and moisture content than larger particles. Also, the maximum decomposition peak was higher for the small particle range. In another research, wheat straw pyrolysis was studied by TGA for seven particle size intervals, ranging from 1.35 mm to 0.150 mm [23]. Higher fixed carbon and volatile matter were found at larger particle sizes, and the char yield increased as the particle size and heating rate of the pyrolysis process increased. More recently, rice straw, pine sawdust, and phoenix tree leaves of various particle size ranges have been tested in TGA [24]. Unfortunately, the ash chemical composition of the samples is not reported, although the ash content is significant (9.72–3.25 % d.b). It is detected that with a reduced particle size of rice straw and pine sawdust, the temperature of the maximum weight loss ratio decreased. In contrast, the opposite behavior is found for phoenix tree leaves, which is attributed to differences in the particle aspect ratio. Since leaves are more flaky-shaped, a denser bed is generated in the reaction device, which increases diffusion resistance.

In the case of gasification, studies dealing with pyrolysis and subsequent non-isothermal gasification are limited, and the impact of the particle size is scarcely reported. In most cases, experimental tests are developed under isothermal conditions and char gasification is conducted separately from pyrolysis after cooling. After char preparation by pyrolysis at various temperatures, heating rates, and holding times (shown in Table 2) the material is usually cooled, crushed, and sieved to the final size. Previous experiences with different coals [26,30] and biomass [25] highlighted that the diffusional effects might be significant for large particle sizes and high temperatures, at which the diffusion reaction regime becomes relevant. At those conditions, the diffusional resistance of the reactant gas into char increases with temperature, and the char gasification reactivity decreases as the particle size increases. In the case of straw residues, isothermal gasification of pyrolyzed flaw straw of various sizes ranging from 0.090 to 0.925 mm was tested, finding a decrease in the reactivity values with an increase in the particle size [27]. However, the ash content of the pyrolyzed char reported was significantly low (2% in d.b.) and the ash composition

Table 1
Main previous research on the influence of particle size distribution on straw pyrolysis.

Material	Particle size	Pyrolysis conditions	Remarks	Reference
Miscanthus	0.12 mm, 1 mm	TGA, Ar, 4 mg, 140 ml/min, 10–40 °C/min, 500 °C	No substantial differences in the thermal decomposition with particle size	[21]
Switchgrass, Reed canary grass	<0.09 mm, 0.09–0.6 mm	TGA, N_2, 3 mg, 20 °C/min, 15 min holding time, 900 °C	Higher concentrations of inorganic and higher moisture content found for smaller particles. Higher carbon, higher volatile, and lower nitrogen content for larger particles.	[22]
Wheat straw	Seven ranges, from 1.35 mm to <0.150 mm	TGA, N_2, 5–20 mg, 45 ml/min, 800 °C	Higher fixed carbon and volatile matter at larger particle sizes. Char yield increased as the particle size and heating rate of the pyrolysis process increased.	[23]
Rice straw, pine sawdust, phoenix tree leaves	0.250–0.380 mm, 0.150–0.180 mm, 0.109–0.120 mm	TGA, N_2, 10 mg, 100 ml/min, 5–40 °C/min, 900 °C	With a decrease in the particle size of rice straw and pine sawdust, the initial and final pyrolysis temperatures and the temperature of the maximum weight loss ratio decreased. The opposite is found for leaves.	[24]

Table 2
Main previous research on the influence of particle size distribution on char gasification.

Material	Pretreatment	Pyrolysis conditions	Char preparation	Gasification conditions	Remarks	Reference
Olive residue	Sieving, 1.41–2.83 mm	Fixed bed, N_2, 900 °C, 30 °C/min, holding time 7 min, cooling	Crushing <0.15 mm, 0.8–1.0 mm, 1–1.4 mm, 1.4–2.8 mm	TGA, 10–28 mg, N_2 to 1000 °C at 30 °C/min, 10 min holding time, cooling from 1000 °C to set temperature (800–950 °C) at 25 °C/min (N_2), char gasification with 0.2, 0.35, and 0.5 bar CO_2 partial pressures	Diffusional effects are important at larger particle sizes	[25]
Rice straw, sawdust	Not specified	Fixed bed, N_2, 850 °C, 25 °C/min, holding time 30 min, cooling	Sieving <0.046 mm, ~ 0.250 mm	TGA, 5 mg, N_2 at 25 °C/min, CO_2 to 850–1300 °C (isothermal), 80 ml/min	Gasification rates are affected by pore diffusion resistance under high temperatures (>1000 °C) and large particle sizes	[26]
Flax straw	Grinding, sieving, <0.090 mm, 0.287 mm, 0.512 mm, 0.725 mm, 0.925 mm	Tubular reactor, N_2, 300 °C (torrefaction), 500 °C (pyrolysis), 8 g, 50 ml/min, 60 min holding time, cooling	Not specified	TGA, 10 mg, N_2, 45 ml/min, 5 min holding time, switch to CO_2, isothermal 750–900 °C, 45 min holding time	A decrease in the reactivity values is observed with an increase in the particle size.	[27]
Wheat straw	Grinding, sieving, 0.925 mm	Tubular reactor, N_2, 10 g, 12 °C/min, 500 °C, 45 min holding time, cooling	Grinding <0.060 mm, 0.250 mm, 0.638 mm, 0.925 mm	TGA, 10 mg, CO_2, 50 ml/min, isothermal 750–900 °C, 45 min holding time	Reactivity increases with temperature, and it decreases as the particle size increases.	[28]
Rice straw	Grinding, sieving, 0.180–0.425 mm	Tubular reactor, N_2, 60 g, 5 °C/min, 300–500 °C, 90 min holding time	Shredding, 0.250–0.380 mm, 0.180–0.250 mm, 0.150–0.180 mm, 0.120–0.150 mm	TGA, 15 mg, N_2 at 25 °C/min, CO_2, 15 mg, isothermal 900 °C	For large particle size, char gasification process is also controlled by heat and mass transfer	[29]

was not reported. In addition, isothermal gasification kinetics of wheat straw char of various particle sizes with CO_2 using TGA were studied, leading to the same conclusions [28]. In those studies, mineral content was not considered a relevant parameter, with the main focus being the particle size influence.

Only recently, non-isothermal CO_2 gasification reactivities of three biomass chars (wheat stalk, rice lemma, and pine sawdust), pyrolyzed at 1100 °C in a fixed bed furnace were compared [31]. The particle size distribution was concentrated in the 0.01–0.05 mm range. Although the particle size of the pine sawdust char was larger than that of wheat straw char and rice lemma-char, the gasification reactivities did not follow the same trend, not aligned with the common knowledge that the reactivity of char increases as the particle size decreases. The authors concluded that in their study the particle size was not the main factor affecting gasification and that the carbon structure of the char may play a significant role in char gasification reactivity. In addition, the non-isothermal gasification of seven types of straw residues with sizes ranging from 0.2 to 0.45 mm was tested [32], finding a positive correlation of the char reactivity with the cellulose content and a negative influence with the lignin content. The weight loss, the maximum weight loss rate, and its corresponding temperature were mainly determined by the fixed carbon content, and the reactivity was correlated with the catalytic ash components.

Given the limited or even contradictory studies, more detailed insight is needed to explore the effects of the chemical heterogeneity of particle size fractions in the pyrolysis and gasification processes. To this aim, a detailed characterization of the biomass precursor is carried out in this paper. Barley straw, a widespread biomass residue, is used as the feedstock material. The raw material is separately sieved, and samples are submitted to complementary analytical techniques to evaluate chemical and textural differences of the raw material before thermal treatments. The study has been completed with detailed non-isothermal thermogravimetric analyses under inert (N_2) and oxidizing (CO_2) atmospheres and several heating rates to evaluate differences in pyrolysis and gasification conversion rates with particle size. Results

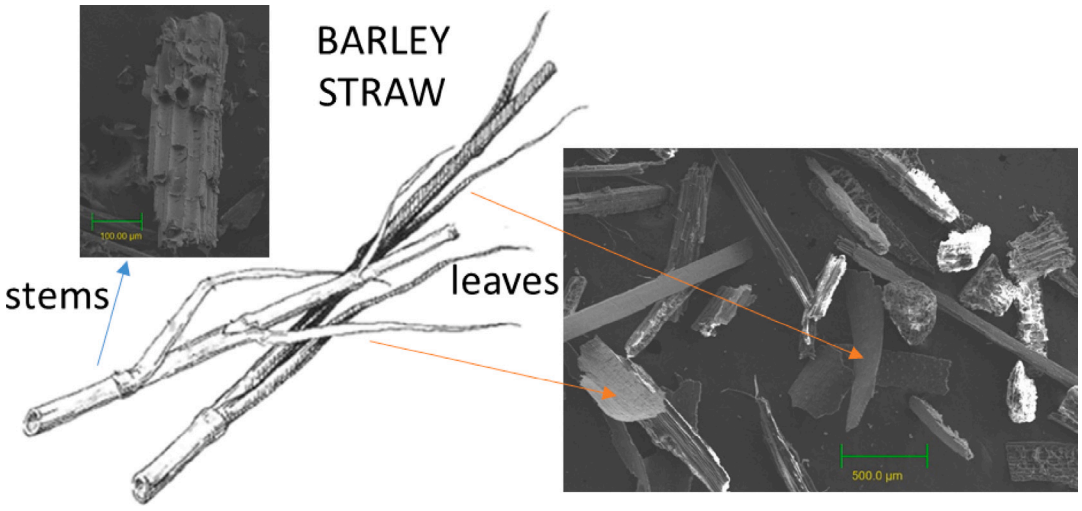

Fig. 1. Main components of straw and selected SEM micrographs from 0.5 mm barley straw after milling.
Source: Adapted from [37].

from the current study may help to design operation strategies to enhance activated carbon quality and prevent ash-related problems.

2. Materials and methods

Barley, a crop with a significant percentage of harvested area in Spain and Europe (42% and 19% in 2021, respectively [33]) has been chosen as the feedstock material. Several studies indicate that 15%–50% of the residual biomass does not have an end-use [34], and there is a need to find other uses to prevent, for instance, straws from being incinerated in the field, causing the emission of pollutants and carbon dioxide. Barley straw is collected during the cereal harvest, spread in the field, gathered, and mechanically packed in bales. Although barley straw bales are mainly composed of cane-shaped stems (80%–90%), the primary and secondary leaves are usually packed together. Fig. 1 sketches the main components of the raw material, showing particles of various sizes and shapes coming from stems and leaves.

A representative sample of the collected bale is oven-dried at 105 °C until its moisture stabilized below 10%. Size reduction by grinding and subsequent classification is carried out in a hammer mill coupled to a vibrating sieve machine at a particle size of less than 0.5 mm. Afterward, the sample is classified with standard sieve meshes to five different size ranges and stored in closed containers. Particle size ranges are labeled from R1 to R5 (from coarse to fine) using standardized mesh screens according to the cumulative size distribution of the ground raw sample. Representative samples are prepared using the standard quartering procedure (UNE-EN ISO 18135:2018). Maximum and minimum intervals and average particle sizes appear in Table 3. Fig. 2 shows the particle size distribution of a representative sample obtained from the closed container after milling and corresponding R1–R5 mass fractions (in %). The resulting distribution depends mainly on the milling device used and the intervals chosen for classification [35]. The R3 interval (0.250–0.150 mm) is the most significant weight in the sample (>35%), which leads to an average size of 0.195 mm. The lowest range (<0.1 mm, R5) concentrates a relevant percentage of the total (20%), consistent with other studies on ground herbaceous straws [36].

Proximate and ultimate analyses are performed in duplicates on each particle size interval (R1–R5) according to EN and ISO standards, shown in Table 4. Major and minor elements are analyzed by Inductively Coupled Plasma Optical Emission Spectrometry (ICP-OES Thermo Elemental IRIS Intrepid).

Surface areas of biomass samples are determined by the gas sorption analyzer ASAP 2020 (Micromeritics), using the Brunauer–Emmett–Teller (BET) method to determine the specific surface area.

Table 3
Biomass size ranges studied.

Sample	Range, mm	Average particle size, mm
R1	0.500–0.355	0.427
R2	0.355–0.250	0.302
R3	0.250–0.150	0.200
R4	0.150–0.100	0.125
R5	<0.100	0.050

Table 4
Standards used in analyses (% wt. dry basis).

Analysis	Equipment	Standard used
Moisture	drying oven	UNE-EN ISO 18134:2016
Volatile matter	furnace	UNE-EN 18123:2016
Ash	furnace	UNE-EN ISO 18122:2016
Fixed carbon		by difference
Ultimate	CHNS Thermoflash 1112	UNE-ISO 16948 2015
		UNE-ISO 16993 2017

The morphology of the samples is studied by Scanning Electron Microscopy and Energy Dispersive X-ray (SEM-EDX), carried out using a Field Emission Scanning Electron Microscope (FE-SEM) Carl Zeiss MERLIN. Observations are conducted on small sub-samples of different size ranges. Three particles are chosen, and micrographs at 5 kV (EHT) and spot elemental EDX analyses at 15 kV are performed. Micrographs are taken with 5-kV electron beam voltage. Initially, a general image is made at 30 magnifications for all samples, then three particles are chosen randomly, and images are captured with magnifications in the 1000 to 50,000. Nearly flat-shaped particles are selected when possible to avoid interference in the measurement. Subsequently, EDX is switched to 15 kV and x 2000 magnification, depending on the view area, and elemental composition analyses are taken at various random points.

The crystalline structures of the samples are also studied by XRD. Data are collected with a diffractometer RIGAKU Ru2500, using CuKα radiation at 40 kV and 80 mA (measurement conditions: 2θ=5° to 80°, step =0.03, t = 1 s/step). Spectrum peaks are analyzed with the JCPDS-2000 database (Joint Committee on Powder Diffraction Standards) to detect crystallographic compounds.

In addition, the influence of particle size and heating rate on pyrolysis behavior is investigated in a thermobalance (Netzsch TG 209F1 Libra). Approximately 7–9 mg of sample is placed in an Al_2O_3 crucible, and non-isothermal TGA tests are performed from room temperature to

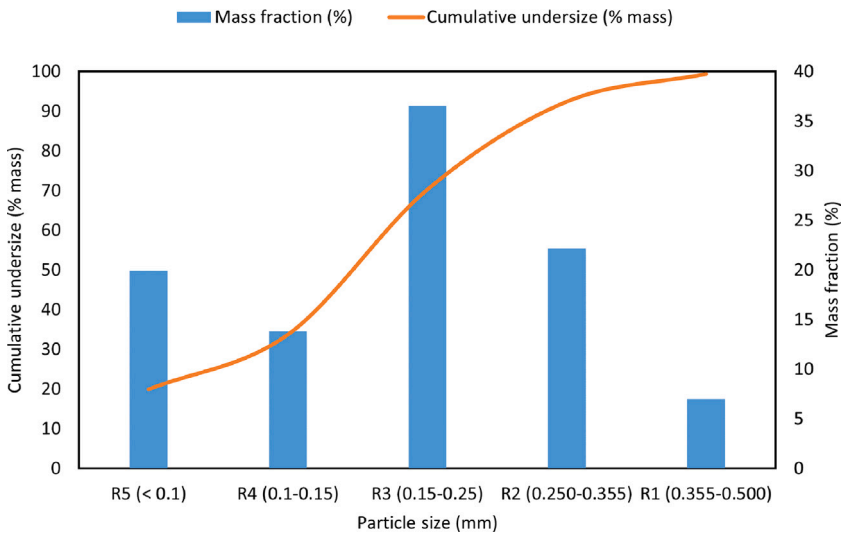

Fig. 2. Particle size distribution of the barley straw sample after milling (UNE-CEN/TS 15149-2 EX).

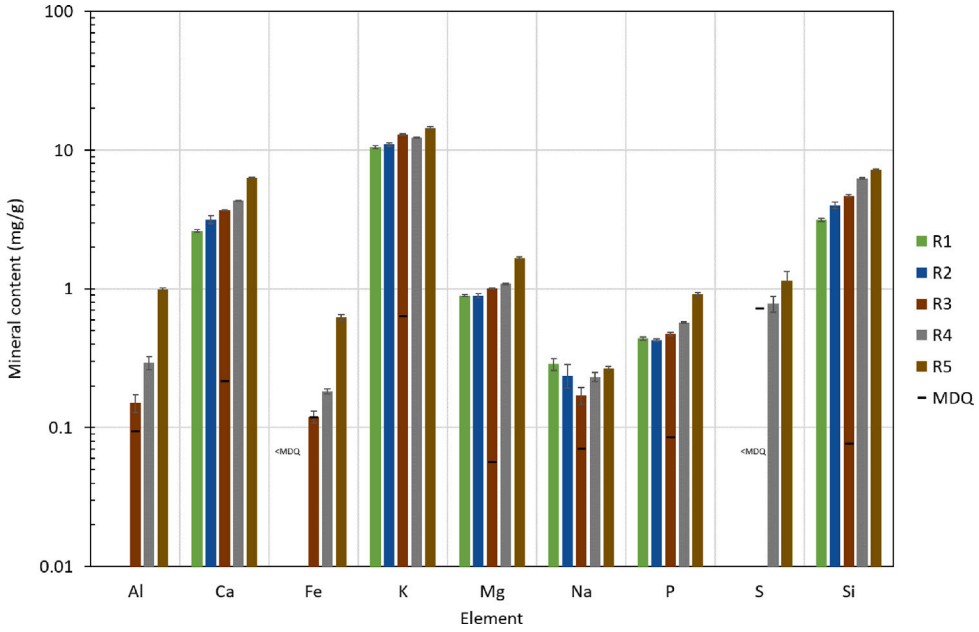

Fig. 3. ICP-OES of the barley straw sample. MDQ — Minimum detectable quantity.

900 °C at five heating rates (5, 10, 15, 20, 30 °C min^{-1}) under an inert atmosphere (N_2). Mass-loss curves against temperature and pyrolysis conversion (V/V*) versus time and temperature are studied in detail. The pyrolysis conversion is defined as $V/V^* = (m_0 - m_t)/(m_0 - m_\infty)$, where m_0 is the initial sample weight at time t_0, m_t is the sample weight at time t, and m_∞ is the final weight at the end of the pyrolysis stage.

Finally, the CO_2 gasification behavior of the biomass samples after N_2 pyrolysis at 500 °C and 1-hour stabilization is evaluated by non-isothermal TGA at three heating rates (5, 10, 15 °C min^{-1}). Experiments are performed on a thermobalance equipped with an opaque Pt crucible (SETARAM SETSYS Evolution 1750) using 19–20 mg of sample. The global conversion is defined similarly to the pyrolysis tests. Conversion of the gasification stage was calculated as $X = (m_{g0} - m_{gt})/(m_{g0} - m_{g\infty})$, where m_{g0} is the initial sample weight at the start of the gasification stage, m_{gt} is the sample weight at time t, and $m_{g\infty}$ is the final weight after gasification. The gas flow rate for all TGA tests is 50 ml·min^{-1}. To obtain the curve of the derivative of the conversion degree, the resulting signal is previously filtered to eliminate the high-frequency noise with the Savitsky–Golay filter using Matlab. This widely used function achieves good results by smoothing the curve while maintaining the integrity of the main peaks [38,39].

The comprehensive gasification characteristic index S has been used to evaluate gasification reactivities among the different particle size fractions. The parameter S, derived from the Arrhenius equation, is used for non-isothermal gasification characterization [31,40]:

$$S = \frac{(dX/dt)_{max} \cdot (dX/dt)_{mean}}{(T_i^2 \cdot T_f)} \quad (1)$$

where $(dX/dt)_{max}$ and $(dX/dt)_{mean}$ represent the maximum and mean gasification rates, in min^{-1}, and T_i and T_f are the initial and final gasification temperatures in K, taken as the temperature at the conversion rate of 0.1 and 0.9, respectively [41].

3. Results and discussion

Proximate and ultimate results are shown in Table 5. In general terms, values are in accordance with other previous works that use barley straw [42,43]. Fixed carbon and volatile matter contents decreased

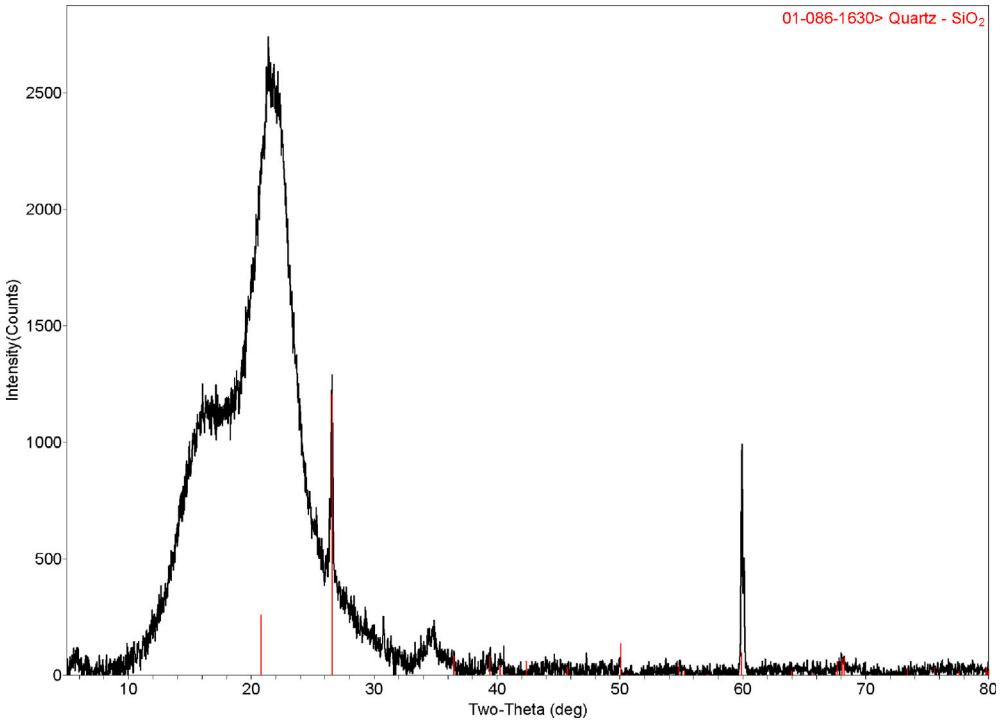

Fig. 4. XRD spectrum of the barley straw sample R5 (<0.1mm) and SiO_2 from JCPDS database (in red).

Table 5
Ultimate, proximate analyses and BET areas of barley straw samples.

Average particle size	Ultimate (wt.%)[a]					Proximate (wt.%)[c]				BET area (m^2/g)
	C	H	N	O[b]	S	M	VM	FC	Ash	
R1 (0.427 mm)	48.0	5.7	0.6	41.7	0.1	8.7	76.8	19.2	4.0	0.69
R2 (0.302 mm)	47.7	5.7	0.8	40.7	0.1	8.8	75.9	19.1	5.0	0.65
R3 (0.200 mm)	47.5	5.7	0.8	40.0	0.1	8.6	75.5	18.6	5.9	0.61
R4 (0.125 mm)	47.1	5.7	0.9	40.2	0.0	8.5	75.3	18.6	6.1	0.70
R5 (0.050 mm)	46.5	5.7	1.3	37.7	0.0	8.4	74.3	16.9	8.8	1.22

M — moisture; VM — Volatile matter; FC — Fixed carbon.
[a]On dry-ash-free basis.
[b]Calculated by difference.
[c]On a dry basis, except for moisture which is on as received basis.

as the particle size was reduced, a similar trend found in [22] for energy crops, but the moisture decreased, in contrast to [22]. The ash content increased from 4.0% (R1) to 8.8% (R5) on a dry basis. As particle size was reduced, carbon and oxygen slightly decreased, and sulfur content was almost zero. Nitrogen content increased for R5, possibly coming from the use of fertilizers. Results also agree with [23], although in the present research, variations of the proximate analyses with particle size are less steep than those reported by the authors for the <0.15mm size range. Although BET areas were very low, they increased for the finest fraction (R5), indicating that for the raw material, microporosity was negligible, being developed during the subsequent processes of pyrolysis and activation [44].

Results of ICP-OES analyses of the raw samples, depicted in Fig. 3 in log scale, agree with proximate. The mineral content (K, Ca, Si, Mg, P) increases from R1 to R5. Minor elements (Al, Fe) are the highest for R5. The most probable reason for the increased presence of aluminum and iron in small sizes is due to exogenous material coming from harvesting, transporting, and storage operations [45,46]. In addition, the presence of crystallographic structures in the samples was examined by X-ray diffraction (XRD). Three characteristic broad diffraction peaks arise at 2θ =18°, 22°, 35°, representing amorphous cellulose [47,48]. In all samples tested, only sylvite (SiO_2) was detected in the finest range (<0.1mm) (Fig. 4), which supports the assumption of exogenous contamination suggested by ICP results. Regarding inorganic elements,

Table 6
Inorganic indexes of raw barley straw as a function of particle size.

Molar ratio	R1	R2	R3	R4	R5
(Si+P+Al)/(Fe+K+Ca+Mg+Na)	0.33	0.38	0.39	0.53	0.52
(Si+P+K)/(Ca+Mg)	3.85	3.78	3.85	3.65	2.92
(Si+P)/K	0.47	0.56	0.55	0.77	0.77
Si/K	0.42	0.51	0.50	0.71	0.69
Si/Ca	1.71	1.81	1.81	2.08	1.64

Table 6 shows results for the barley straw samples calculated from ICP-OES. An increase in (Si+P+Al)/(Fe+K+Ca+Mg+Na), (Si+P)/K, and Si/K ratios is observed for R4 and R5 size fractions, mainly due to the increase of Si content when particle size is decreased. Given the results, a certain tendency to lower gasification reactivities would be expected for the small fractions.

3.1. SEM-EDX analyses

Figs. 5, 6, and 7 illustrate relevant SEM micrographs of R1, R3 and R5 samples, respectively (R2 and R4 images are not shown for conciseness). R1 and R3 images were captured at a magnification scale of x30 (Figs. 5(a) and 6(a)), whereas R5 (Fig. 7(a)) was taken at 50x.

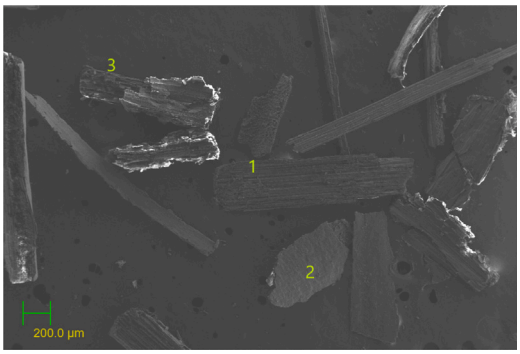

(a) R1 sample at 30x magnification

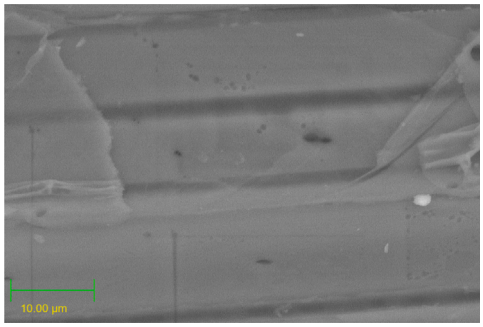

(b) EDX at 2000x. Particle no. 1 (stem)

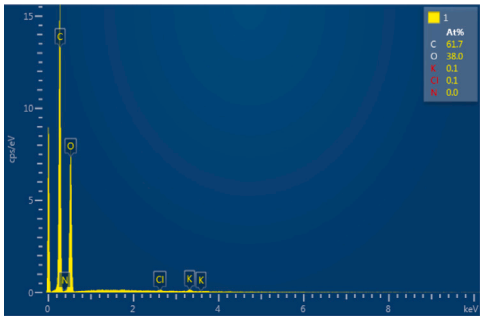

(c) EDX global spectrum. Particle no. 1

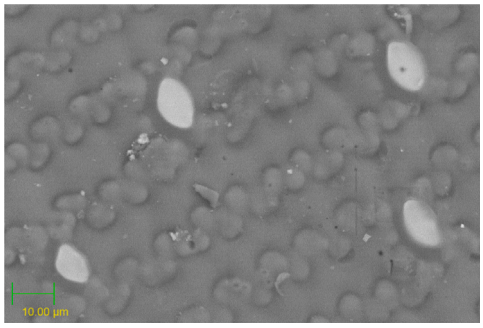

(d) EDX at 2000x. Particle no. 2 (leaf)

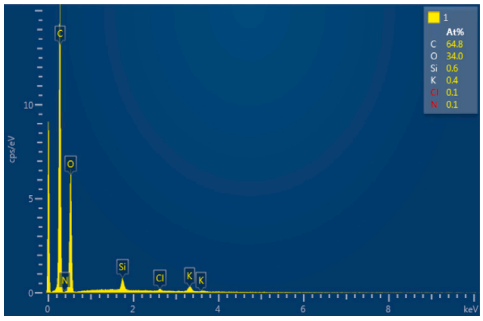

(e) EDX global spectrum. Particle no. 2

Fig. 5. SEM-EDX images and corresponding spectrum of selected particles (1-2) in R1 (0.500–0.355 mm).

differences in particle shapes arise upon careful examination of pictures. Although particle size follows the expected trend (R1>R3>R5), particles larger than the sieve size appear in the figures. The classification method based on standard sieves generates larger barley straw particles; hence, the average particle size calculated from each range is approximate. The heterogeneity of the samples is evident from the images. Particles of various shapes and sizes can be identified as part of stems (1), with an inner tubular and elongated structure, common to herbaceous-type biomass, leaves (2), striated and with clearly visible stomata and xylem tissues, and long needles from spikes (3). Corresponding particles are labeled as 1, 2, and 3 in Fig. 6(a). These structures are common to all samples studied and may result in variations in the thermal evolution during pyrolysis and activation stages due to their different aspect ratios.

Some regions of EDX images in R1, R3 and R5 have been selected for performing elemental analyses (shown in Figs. 5(b)–5(e), 6(b)–6(g) and 7(b)–7(g), elements in at.%). Results of EDX qualitatively agree with ICP-OES. In the case of R1, particles labeled as 1 and 2 in Fig. 5(a) were identified as parts of stems and leaves, respectively (Figs. 5(c)–5(c)). They have low Cl and K contents, and Si is slightly detected in particle 2 (Fig. 5(e)), clearly seen in Fig. 5(d) as disk-shaped particles, probably coming from stomata. As the size is reduced, particles are also enriched in inorganic elements, such as Si, Ca, Mg, and Fe (Fig. 6(d)). It is worth noting the increased Si content in particle no. 2 in R3 (Figs. 6(c)–6(g)) and R5 (Fig. 7(e)), which are parts of a barley leaf.

3.2. Pyrolysis tests

Thermal decomposition profiles of barley straw samples are shown in Figs. 8(a)–8(c) as a function of particle size at 5, 15, and 30 °C min^{-1}, respectively. As expected, they exhibit the typical biomass evolution [49], with moisture loss above 100 °C, and hemicellulose decomposition above 300 °C. The peak of cellulose decomposition appears at 350 °C. Lignin zone is wider than the others and extends beyond 500 °C. Previous analyses of hemicellulose, cellulose, and lignin to barley straw samples show contents of 35.1%, 46.6% and 15.7%, respectively, in dry extract and washed with water [50]. The corresponding peak is less pronounced as hemicellulose content is smaller than cellulose. The shape and peaks of the curves are very similar for the different size ranges. However, for fraction R5, it is observed that the peak of the cellulose decomposition has a lower height and occurs at a slightly lower temperature. The opposite effect is observed for R1.

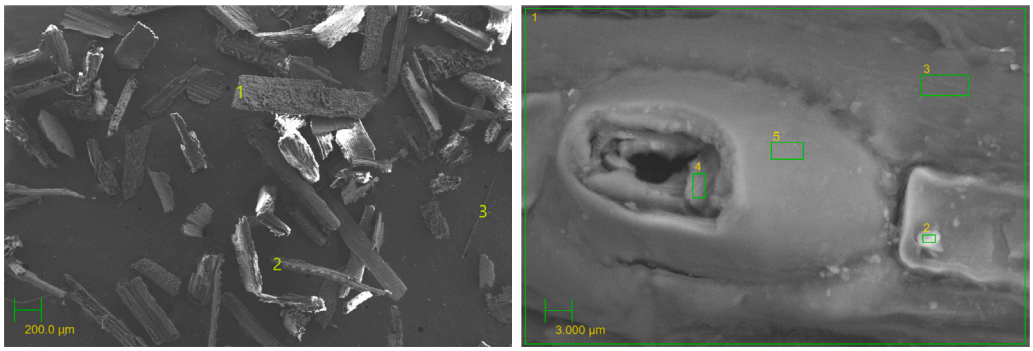

(a) R3 at 30 x magnification (b) EDX at 2000x. Particle no. 2 (leaf)

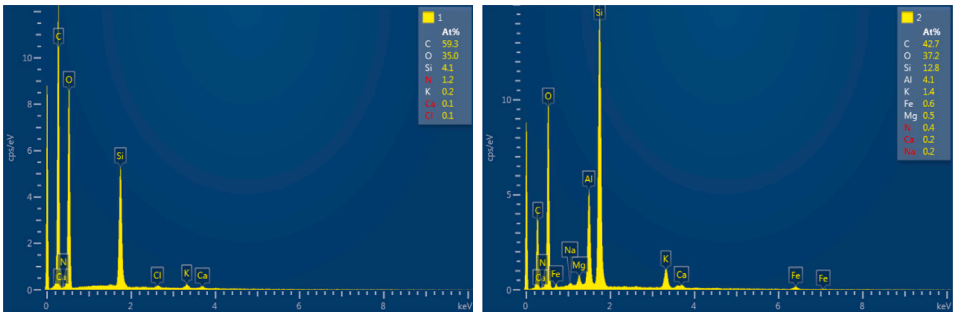

(c) EDX spectrum. Particle no. 2. Zone 1 (d) EDX spectrum. Particle no. 2. Zone 2

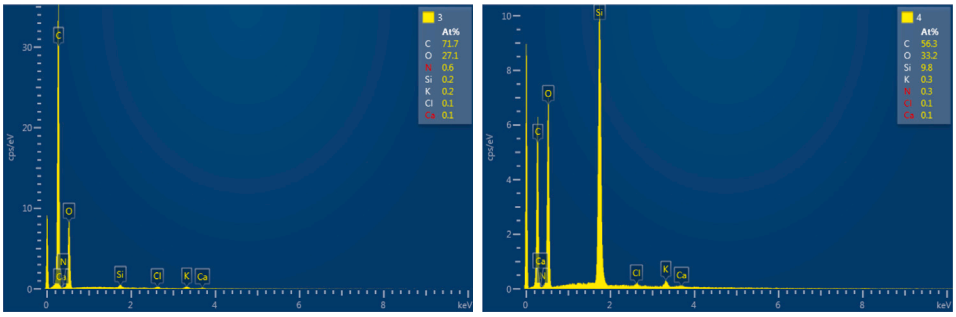

(e) EDX spectrum. Particle no. 2. Zone 3 (f) EDX spectrum. Particle no. 2. Zone 4

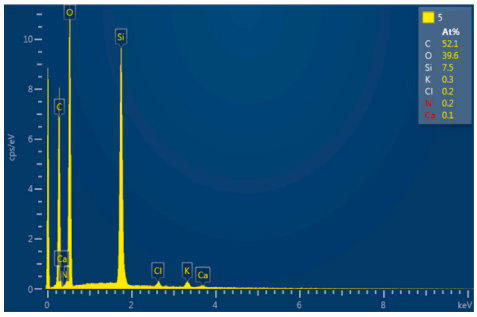

(g) EDX spectrum. Particle no. 2. Zone 5

Fig. 6. SEM-EDX images and corresponding spectrum of selected particles in R3 (0.250–0.150 mm).

As the heating rate (HR) increases, the curves move to the right, which means that the maximum mass loss occurs at a higher temperature. Such an effect is caused by changes in the reaction mechanism by increasing the heating rate due to thermal inertia and different heat dissipation or absorption rates in the sample [51,52]. It is also observed that the width of the primary or active pyrolysis zone is greater as the heating rate increases. Above 400 °C, the slope of the lignin decomposition zone becomes greater at a higher heating rate, similar to other works [52]. Figs. 9(a)–9(c) illustrates the evolution with the temperature of the derivative curve for R1, R3, and R5 size fractions as a function of the heating ratio. R2 and R4 curves are not shown for conciseness. The catalytic action of AAEM is reflected in the curves of thermal decomposition by size fractions. If we compare Fig. 9(a) with Fig. 9(c), it is observed that the peak widths are smaller for R5, and occur at lower temperatures. The hemicellulose "shoulder" disappears for R5, which is attributed to the action of potassium [52]. Another in-depth study on the effect of inorganic salts on biomass pyrolysis states that inorganic salts of alkali metals can catalyze cellulose and hemicellulose fragmentation by reducing the activation energy [53,54]. Phosphorus facilitates the complete decomposition of biomass [55]

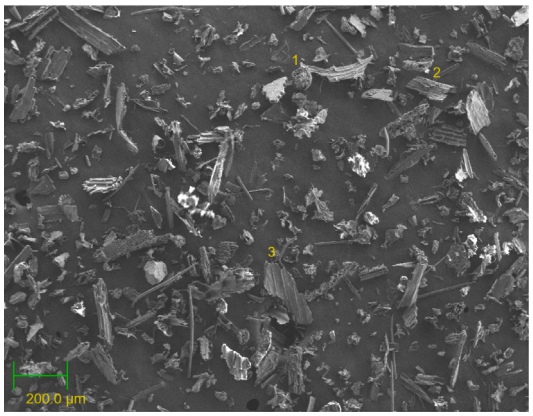

(a) R5 sample at 50x magnification

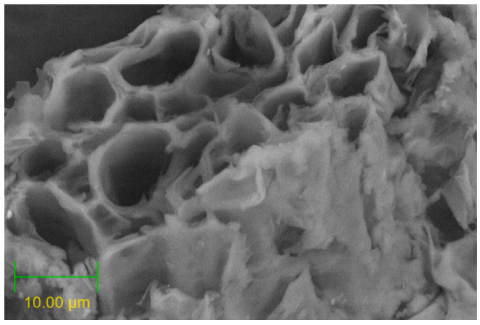

(b) EDX at 2000x. Particle no. 1 (stem)

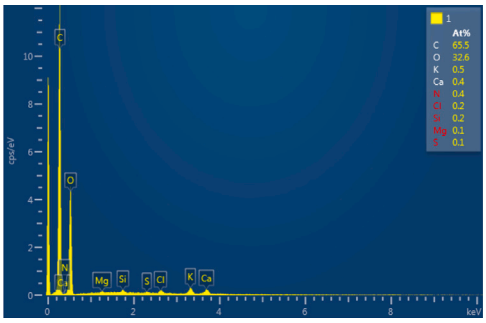

(c) EDX global spectrum. Particle no. 1

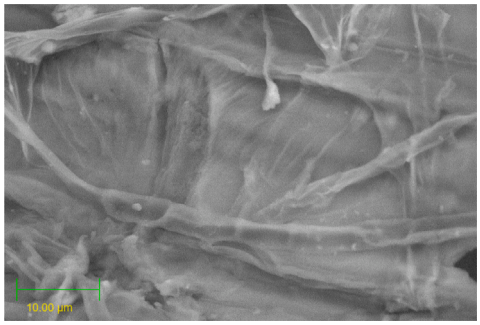

(d) EDX at 2000x. Particle no. 2 (leaf)

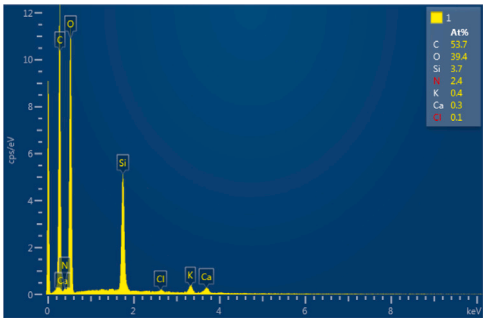

(e) EDX global spectrum. Particle no. 2

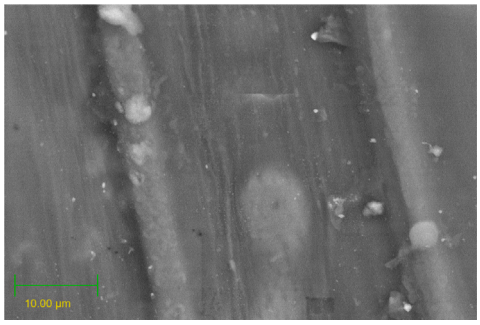

(f) EDX at 2000x. Particle no. 3 (leaf)

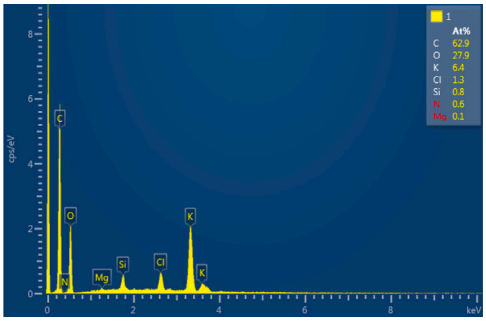

(g) EDX global spectrum. Particle no. 3

Fig. 7. SEM-EDX images and corresponding spectrum of selected particles in R5 (<0.1mm).

whereas silicon, on the other hand, is a more stable element. In addition to the effects of particle size, this could explain the observed effect of the temperature decrease of R5 (<0.1mm). To better appreciate the influence, maximum temperatures of cellulose thermal decomposition have been calculated as a function of particle size and heating rate. As shown in Fig. 10(a), peak temperatures decreased with particle size for all heating ranges (Fig. 10(a)), in accordance with recent findings [24]. Although the mass percentage remaining at 500 °C exhibits a greater dispersion with particle size, the general trend shown in Fig. 10(b) indicates that the percentage of residual mass at 500 °C is greater as the particle size decreases and depends on the amount of ash, which decreases with particle size. At 500 °C, the lignin decomposition

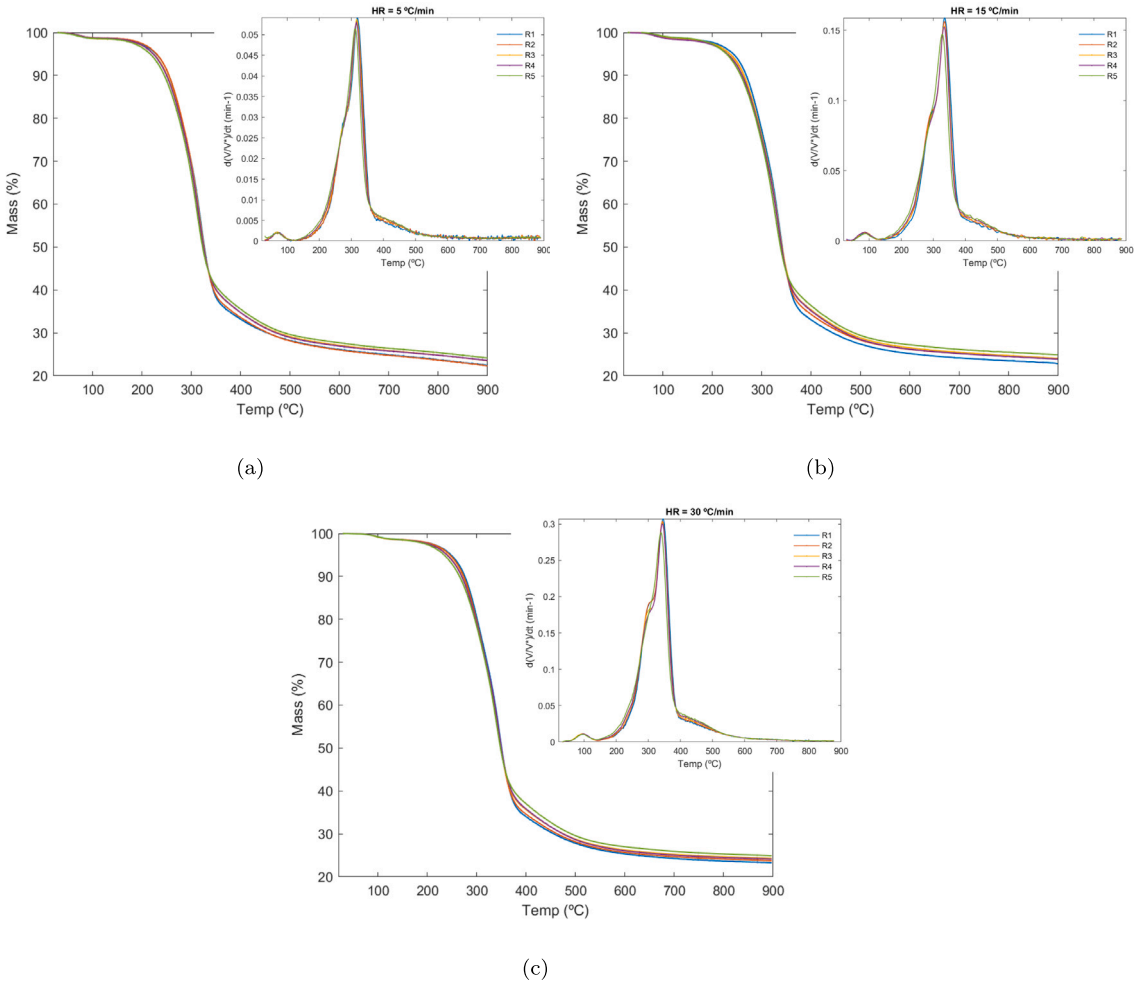

Fig. 8. Mass loss (%) and pyrolysis conversion rate evolution with temperature as a function of the particle size (R1–R5). Heating rate (HR) =5 °C min^{-1} (a), HR =15 °C min^{-1} (b), and HR=30 °C min^{-1} (c).

continues, and differences in lignin contents among size ranges may lead to these variations. The residual mass percentage at the end of the pyrolysis process (Fig. 10(c)) positively correlates with the sum of ash and fixed carbon (in dry basis) found in proximate analyses (Table 5). Finally, a lower residual mass loss at the end of pyrolysis is detected at 5 °C min^{-1} (Fig. 10(c)), caused by an enhanced lignin decomposition in the 500–900 °C interval.

3.3. Gasification tests

Results of TGA tests of non-isothermal CO_2 gasification are shown in Figs. 11–14. Mass loss curves and conversion rates versus particle size for the intermediate heating rate (10 °C min^{-1}) are presented in Figs. 11(a) and 11(b), respectively. Firstly, as expected, pyrolysis curves up to 500 °C follow an almost identical pattern to the previous pyrolysis tests (Section 3.2), which confirms test reliability. The lowest weight loss in the pyrolysis zone occurs for R5, and the greatest for R1, a trend maintained during the subsequent stabilization and gasification processes. The cause may be related, as aforementioned in the previous section, to the lower volatile content, lower fixed carbon, and higher ash content of the R5 fraction compared to R1. Secondly, the mass remains nearly constant during the hold-up period at 500 °C. After the atmosphere changes from N_2 to CO_2, there is a sharp peak in the conversion derivative curves (Fig. 11(b)), attributed to the effect of the pressure when changing bottles [10]. The third stage of TGA tests is the char CO_2 gasification, plotted separately in Figs. 12–14 for 5, 10, and 15 °C min^{-1} heating rates, respectively. The graphs show low conversion values (X <0.1) up to 650–700 °C, increasing sharply from 700 °C. The reaction rate is higher for R5 at low temperatures and heating rates (Fig. 12). The order of the slopes (from highest to lowest) is R5>R4>R3>R2>R1. Beyond that temperature, the reaction rate for R4 and R5 sizes steeply slows down, and the slope order is reversed. The maximum of the dX/dt-X curve is achieved for the R1 size fraction at a conversion level of 0.8–0.9, depending on the heating rate. The reaction zones of R5 and R4 are wider, which indicate a slower mean reaction rate. In the case of 5 °C min^{-1} thermograms (Fig. 12), the gasification reaction ends at lower temperatures. At temperatures close to 850 °C, conversion has reached 100%. The shapes of the curves remain similar to those of 10 °C min^{-1}. However, for 15 °C min^{-1} (Fig. 14) reaction is only completed for the R1 and R2 ranges (Fig. 14).

The different char preparation procedures and previous pyrolysis conditions found in related literature make strict comparison difficult. Nonetheless, apart from the differences, in general, the evolution of gasification conversion rates for R1, R2, and R3 size ranges qualitatively agrees with other related works dealing with non-isothermal biochar CO_2 gasification [40,56–58], showing a three-stage curve and a single peak in the gasification reaction rate with conversion. However, in the present research, smaller fractions, such as R4 and R5, experience a significantly lower mean gasification rate.

In other studies, the CO_2 gasification of a demineralized husk char was compared to its corresponding original char (high in amorphous SiO_2) at the same non-isothermal conditions [56], showing an important increase of the reactivity for the former. The removal of SiO_2 increased the concentration and accessibility of active metallic species,

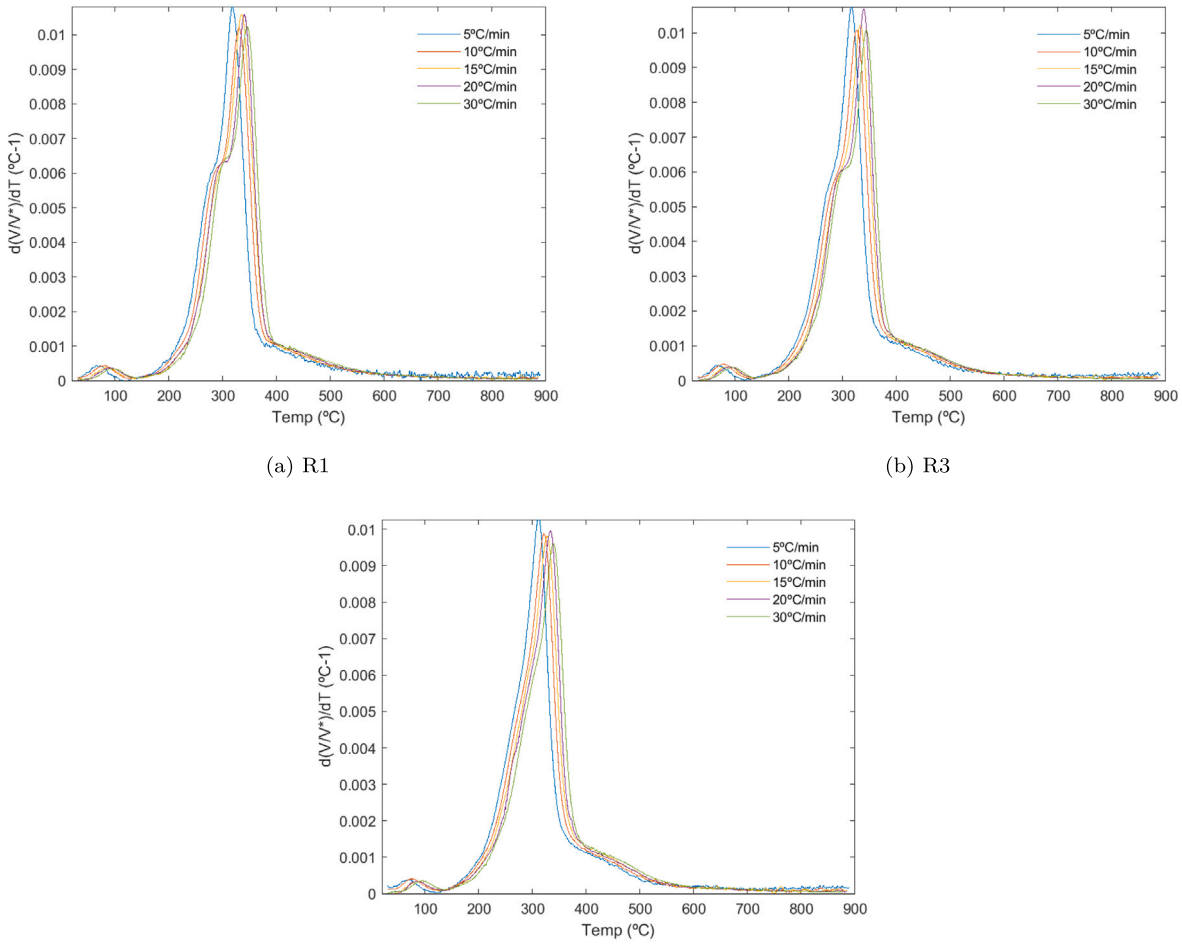

(a) R1

(b) R3

(c) R5

Fig. 9. Pyrolysis conversion rate for R1 (a), R3 (b), and R5 (c).

promoting the reactivity of the char. More recently, non-isothermal gasification of different straw residues has been tested in [32], showing a positive correlation with catalytic ash components.

In consequence, apart from the differences in the development of the char structure in previous stages, the reason for the different behavior among size fractions at lower temperatures and conversion degrees is caused by the catalytic influence of K and Ca, together with the greater heat and mass transfer rates of R4 and R5, due to the smaller size. Inorganic species retained in the char during the pyrolysis stage are important in determining char reactivity. Water-soluble inorganic elements such as K or Na are released from the char at temperatures above 700 °C, while Mg and Ca are more slowly released [59]. Potassium is the most active element among AAEM and may potentially act as an active and fixed element for char gasification unless deactivated by reactions with silica or alumina [60]. In addition, the chemical interactions of potassium species with other inorganic species in char, such as CaO, Al_2O_3, SiO_2, and their compound oxides can also influence catalytic gasification. Therefore, small particles, which have a higher presence of inorganic elements, experience a higher rate of reaction at low temperatures by K or Ca catalysis but a lower rate at high temperatures, hindered by the presence of Si, which would act as an inhibitor [61]. This effect was previously detected in fixed-bed tests with the same material [44]. In this way, the conversion rate evolution for R4–R5 seems to be related to the increase of the Si molar ratios calculated in Table 6.

To evaluate the heating rate effect, conversion rate profiles of R1–R2 and R3–R5 char-CO_2 gasification are depicted in Figs. 15(a)–15(b) and Figs. 16(a)–16(c), respectively. At a fixed particle size, the increase of the heating rate shifts conversion-temperature curves to the right, meaning that the reaction temperature is increased for the same char conversion. The same behavior has also been detected in the pyrolysis curves (9) and in previous gasification studies, such as [57,62]. The effect is caused by heat and mass transfer limitations due to the large energy requirement for the Boudouard reaction since higher heating rates hinder the effective heat transfer to the inner parts of the particles. Moreover, the influence of Si-inhibition is also observed in the R3–R5 size fractions, showing a decrease in the reaction rate at conversions greater than 0.3 (Figs. 16(a)–16(c)).

To quantitatively analyze differences among sizes and compare gasification reactivities, Table 7 shows relevant figures of non-isothermal tests, which confirms previous findings. The heating rate causes a slight increase in the initial, peak, and final temperatures (T_i, T_{peak}, T_f, respectively), and a gradual increase in $(dX/dt)_{max}$, $(dX/dt)_{mean}$, and S values, decreasing the reaction time, t_R. As a consequence, the gasification reactivity is improved at higher heating rates. Trends align with those reported by [31,40,58]. The different materials and pyrolysis conditions influence gasification index S, and a wide range is observed ($S \sim 10^{-11}$–10^{-13}). For comparison, some experimental tests from [58] similar to the present work (miscanthus char, previously pyrolyzed with N_2 at 600 °C, and one hour of holding time) are also included in Table 7. Unfortunately, the char size was not reported in the paper. As seen in the table, the authors obtained slightly lower char reactivities, probably due to the different feedstock characteristics and char preparation temperatures (600 °C vs. 500 °C in our study).

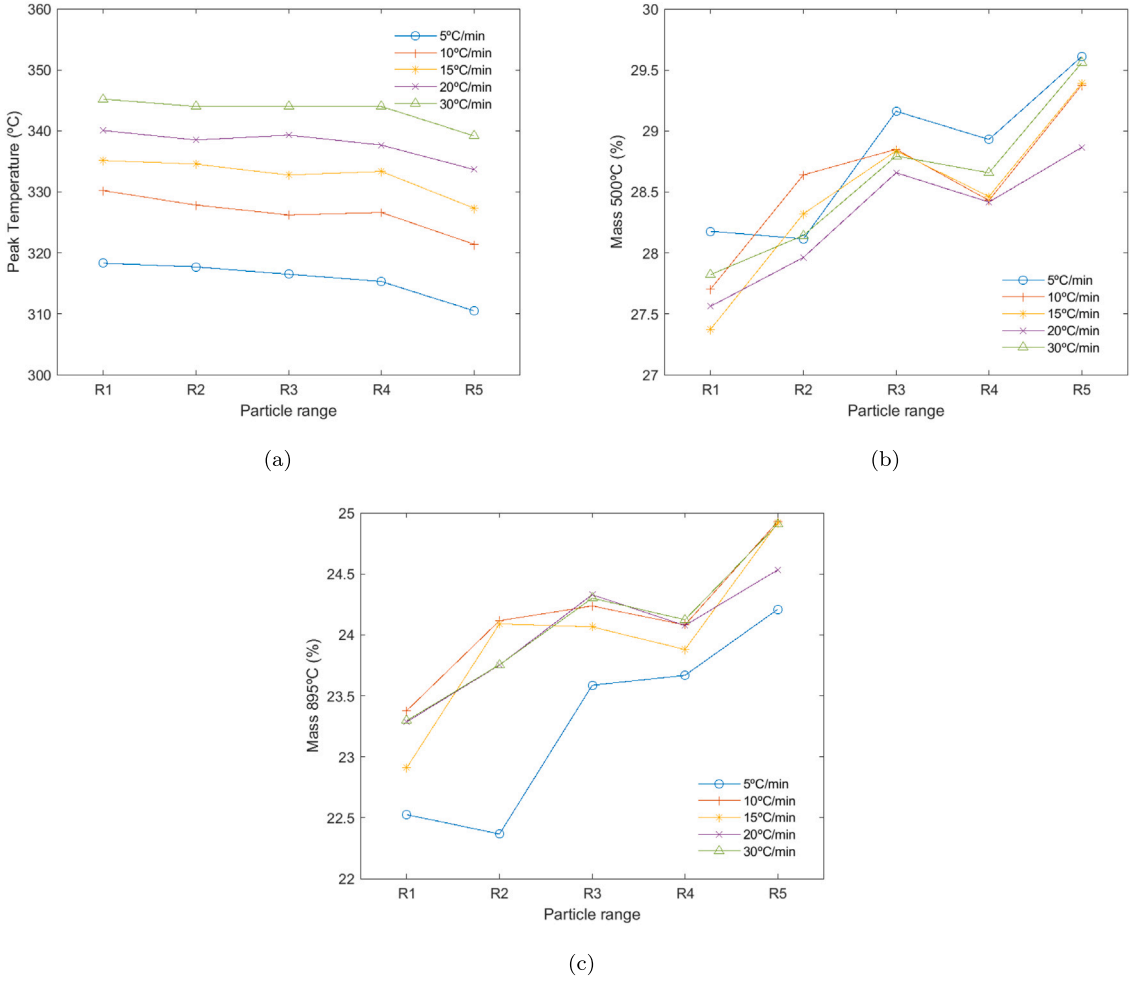

Fig. 10. Cellulose decomposition peak temperature (a), and residual mass % at 500 °C (b) and 895 °C (c) for TGA pyrolysis tests as a function of particle size and heating rate.

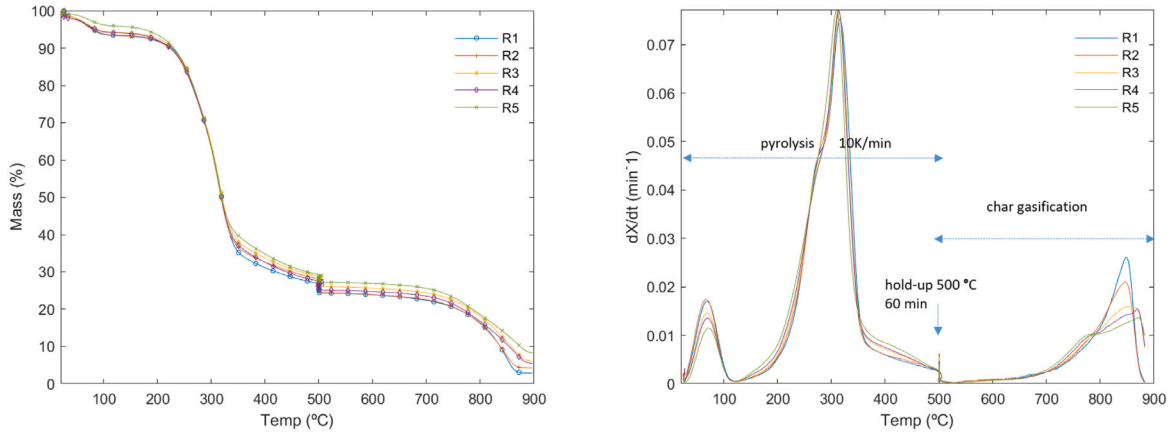

Fig. 11. Global thermograms for HR=10 °C min^{-1} pyrolysis, stabilization and in situ CO_2 char gasification, as function of particle size ranges R1–R5 (here, X is the global conversion $X = (m_0 - m_t)/(m_0 - m_\infty)$).

Higher pyrolysis temperatures are known to decrease char reactivity by decreasing surface-oxygen complexes, which behave as active sites of the gasification reaction [63].

Table 7 also highlights the previously reported differences among particle size fractions. At the start of the gasification process, small particle sizes exhibit lower initial gasification temperatures (T_i), as well as higher conversion rates (Figs. 12(b), 13(b), 14(b)) which agrees with the general trend stating that fine sizes exhibit higher gasification rates. However, as the reaction proceeds, T_{peak} and T_f increase for fines, and the opposite is found for $(dX/dt)_{max}$, $(dX/dt)_{mean}$ and S, meaning that the reactivity is lower for fines and it decreases as the heating rate increases. This effect is shown in Fig. 17(a), where

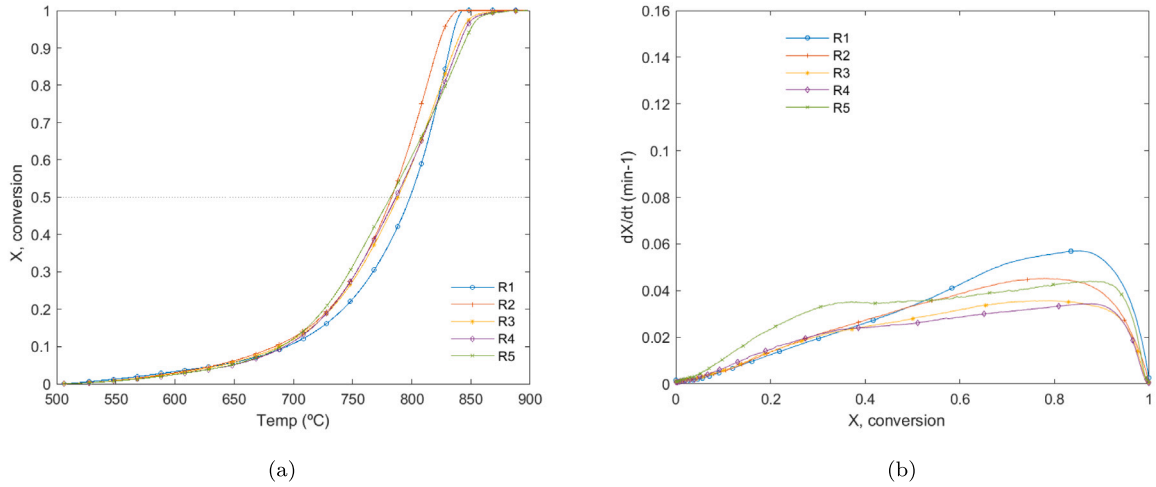

Fig. 12. Char CO_2 gasification at 5 °C min^{-1} heating rate.

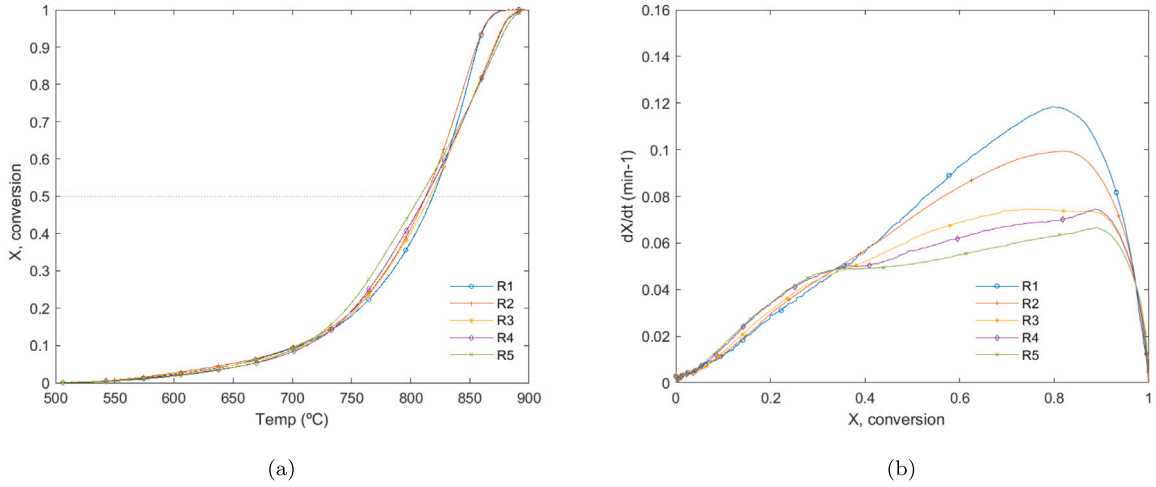

Fig. 13. Char CO_2 gasification at 10 °C min^{-1} heating rate.

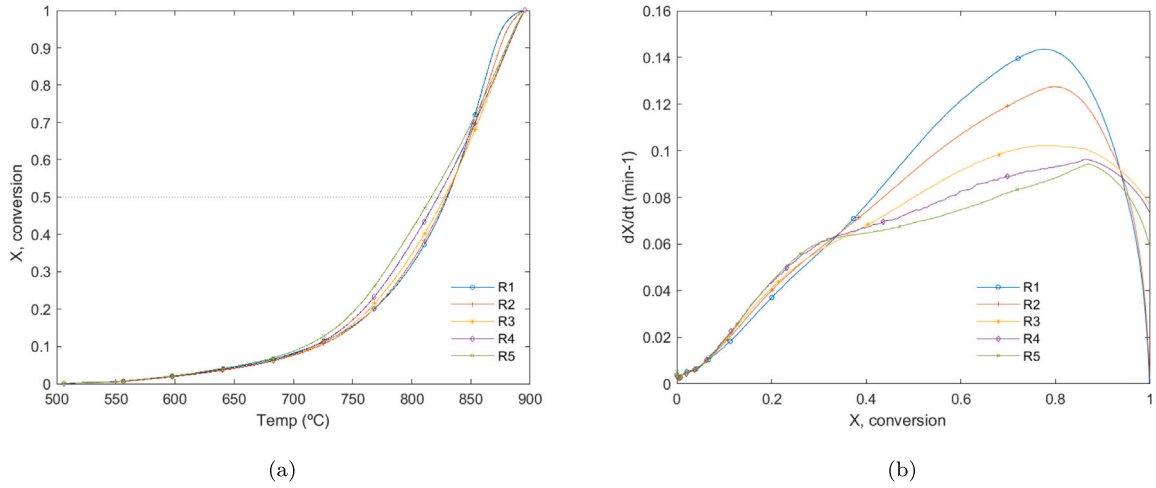

Fig. 14. Char CO_2 gasification at 15 °C min^{-1} heating rate.

the gasification characteristic index S is plotted as a function of the particle size range and heating rates, obtaining R1>R2>R3>R4>R5 for all heating rates. The S-trend is mainly caused by the influence of the maximum conversion rate, $(dX/dt)_{max}$, on S, which increases with particle size and heating rate. As aforementioned, the higher Si/K ratios of small particles produce low-melting compounds, which increases intra-particle (pore) diffusion resistance to heat and mass transfer, causing a decrease in the conversion rate at higher temperatures. On

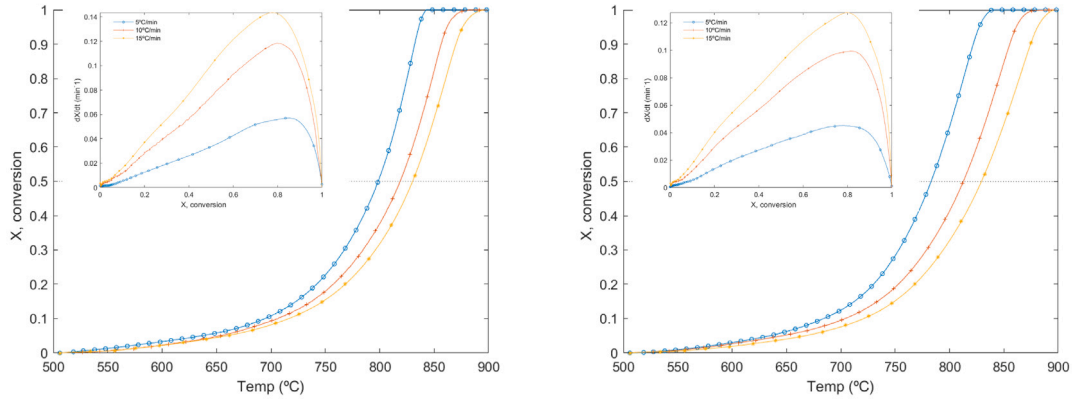

(a) (b)

Fig. 15. Char CO_2 gasification conversion for R1 (a), R2 (b) for the different heating rates.

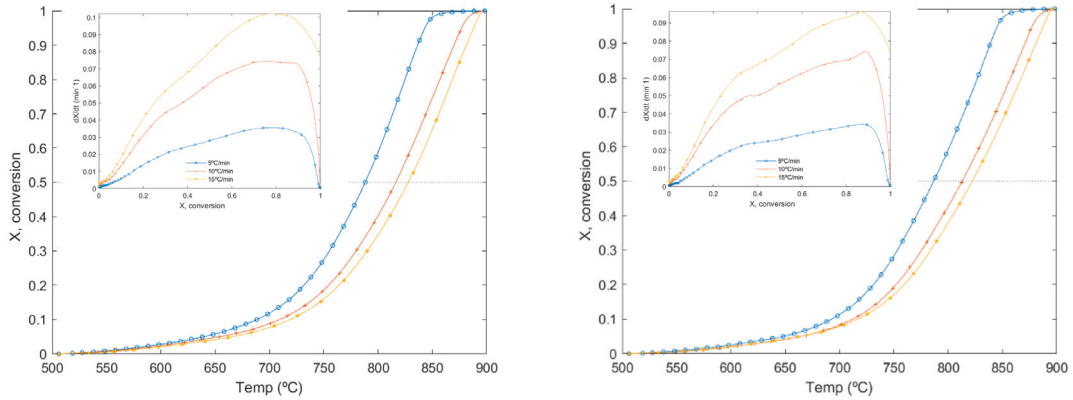

(a) (b)

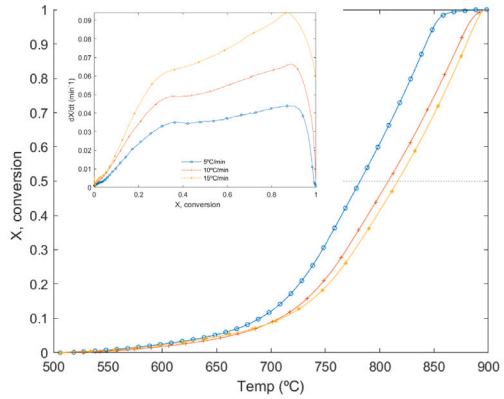

(c)

Fig. 16. Char CO_2 gasification conversion for R3 (a), R4 (b), and R5 (c) for the different heating rates.

the contrary, larger particles have lower Si/K contents and higher fixed carbon contents, which develop a more active char surface area during gasification, leading to higher reactivities. Due to the higher aspect ratio of larger particles, an enhanced inter-particle diffusion may also favor the process. An inverse relationship of the gasification index S with the inorganic molar indexes can be inferred when comparing Figs. 17(a) and 17(b).

Finally, it can be concluded that the effect of size fractionation is significant for non-isothermal char-CO_2 gasification of barley straw. Differences observed are caused, apart from the different char structure development during the pyrolysis and stabilization stages, by the different chemical compositions among size fractions. Larger sizes containing higher carbon and lower ash contents, exhibit faster gasification rates, whereas small sizes, enriched in Si, show poorer gasification

Table 7
Non-isothermal CO_2 char gasification parameters of the samples.

Average particle size	HR (°C min^{-1})	T_i °C	T_{peak} °C	T_f °C	$(dX/dt)_{max}$ min^{-1}	$(dX/dt)_{mean}$ min^{-1}	$t_R=t_i-t_f$ min	S (10^{-12}) min^{-2} K^{-3}
R1	5	695.1	828.4	832.8	0.073	0.029	27.6	2.05
0.427 mm	10	706.0	851.7	856.5	0.127	0.053	15.0	6.26
	15	716.3	860.3	870.0	0.171	0.079	10.2	12.02
R2	5	684.6	813.2	822.7	0.057	0.029	27.6	1.64
0.302 mm	10	703.8	845.5	855.4	0.105	0.053	15.1	5.18
	15	720.9	868.2	874.6	0.149	0.079	10.2	10.03
R3	5	688.2	821.6	836.4	0.045	0.027	29.7	1.18
0.200 mm	10	709.2	848.9	869.9	0.079	0.050	16.1	3.55
	15	718.7	867.5	881.3	0.122	0.074	10.8	7.95
R4	5	692.4	836.6	838.9	0.044	0.027	29.3	1.16
0.125 mm	10	711.9	872.2	870.9	0.078	0.050	15.9	3.54
	15	716.4	880.7	880.9	0.113	0.073	11.0	7.30
R5	5	689.5	842.6	842.5	0.037	0.026	30.6	0.94
0.050 mm	10	707.4	875.2	872.9	0.067	0.048	16.6	3.04
	15	709.4	881.2	879.7	0.112	0.071	11.3	7.14
Miscanthus	5	635.0	894.0	945.0	0.035	0.004	–	0.15
600 °C char	10	690.0	960.0	1006.0	0.059	0.009	–	0.43
[58]	20	701.0	1042.0	1093.0	0.098	0.017	–	1.27

Note: HR, Heating Rate; T_i, initial gasification temperature; T_{peak}, peak conversion rate temperature; T_f, final gasification temperature; $(dX/dt)_{max}$, maximum value of gasification rate; $(dX/dt)_{mean}$, mean value of gasification rate; t_R, time from final conversion (X=0.9) to initial conversion (X=0.1); S, gasification characteristic index.

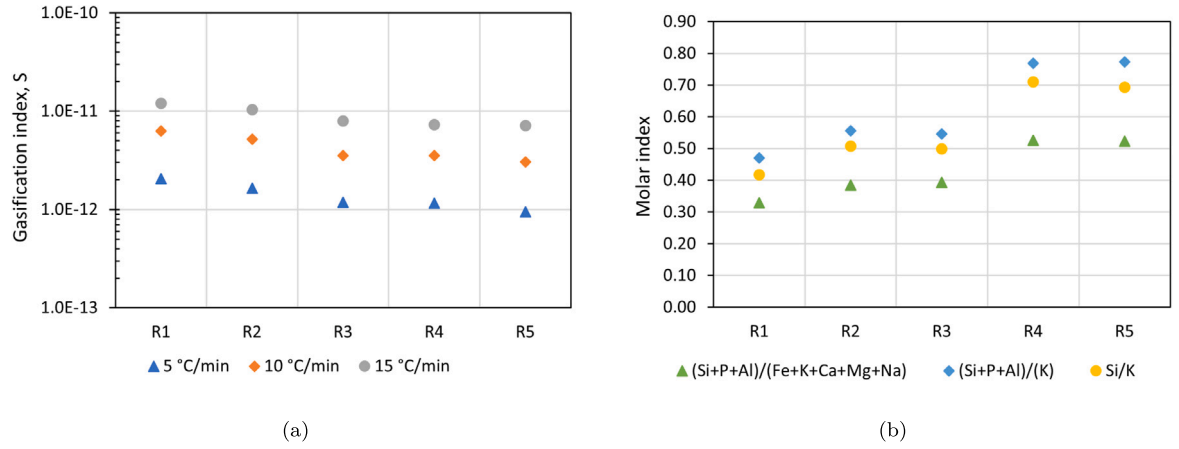

Fig. 17. Influence of particle size on gasification characteristic index S (a), and inorganic molar indexes (b).

performance. Since the different behavior may negatively impact the activation process, prior separation of the Si-rich fractions of the plant before thermal treatments or rejection of the smaller sizes should be advisable.

4. Conclusions

In this paper, size fractionation of barley straw is conducted to study how the heterogeneity of the raw biomass can influence pyrolysis and CO_2-gasification behavior aimed at activated carbon applications. The work has confirmed previous findings and revealed new aspects dealing with particle size. The main contributions are summarized below.

- The study has shown the variability in raw biomass samples obtained after milling and sieving. As the particle size range is reduced, it is significantly enriched in inorganics whereas VM and FC are lower. The increase of inorganic elements found in the finest fraction is caused by exogenous contamination, and an accumulation of Si-K-Cl-rich barley leaves from the original plant by the milling operation since soft tissues are more easily ground.
- Pyrolysis tests exhibit slight differences among size ranges. The higher alkali content of the finest particles favors cellulose and hemicellulose thermal decomposition. The maximum temperature of cellulose decomposition decreases at smaller particle sizes and lower heating rates are caused by their increased heat and mass transfer effects at smaller sizes. The residual mass percentage is greater as the particle size decreases, consistent with the increased ash content of the finer fraction.
- In non-isothermal char CO_2-gasification tests, relevant differences, not previously addressed, arise for the smallest range (<0.15mm), for which the reaction rate decreases at T >750 °C, attributed to the inhibit tendency of silicates, which hinder the reaction at higher temperatures by blocking the pores by forming low-melting potassium-silicates. The gasification index S increases with the heating rate and is inversely related to molar Si-alkali ratios.
- Size fractionation is relevant to the char-CO_2 gasification process, presenting higher conversion rates and lower maximum peak temperatures the larger the particle size. The impact of the ash-forming elements is more relevant than the effect of particle size. These findings are useful in developing operational and pretreatment strategies to improve activated carbon quality.

CRediT authorship contribution statement

Antonia Gil: Conceptualization, Methodology, Investigation, Writing – original draft, Writing – review & editing. **Javier Pallarés:** Conceptualization, Methodology, Validation, Funding acquisition, Project administration, Writing – review & editing. **Inmaculada Arauzo:** Conceptualization, Supervision, Writing – review & editing. **Cristóbal Cortés:** Conceptualization, Supervision, Writing – review & editing.

Declaration of competing interest

The authors declare that they have no known competing financial interests or personal relationships that could have appeared to influence the work reported in this paper.

Data availability

Data will be made available on request.

Acknowledgments

The work presented in this paper has been funded by the Spanish RDI program (RTI2018-095349-A-I00), co-funded by the European Union. Authors would like to acknowledge the use of Servicio de Apoyo a la Investigación-SAI, University of Zaragoza and Instituto de Carboquímica (ICB) for their assistance in the physical and chemical characterization of the materials.

References

[1] A.M. Dehkhoda, N. Ellis, E. Gyenge, Electrosorption on activated biochar: Effect of thermo-chemical activation treatment on the electric double layer capacitance, J. Appl. Electrochem. 44 (1) (2014) 141–157, http://dx.doi.org/10.1007/s10800-013-0616-4.

[2] M.A. Yahya, Z. Al-Qodah, C.W. Ngah, Agricultural bio-waste materials as potential sustainable precursors used for activated carbon production: A review, Renew. Sustain. Energy Rev. 46 (2015) 218–235, http://dx.doi.org/10.1016/j.rser.2015.02.051.

[3] S. Schaefer, G. Muñiz, M.T. Izquierdo, S. Mathieu, M.L. Ballinas-Casarrubias, G. González-Sánchez, A. Celzard, V. Fierro, Rice straw-based activated carbons doped with SiC for enhanced hydrogen adsorption, Int. J. Hydrogen Energy 42 (16) (2017) 11534–11540, http://dx.doi.org/10.1016/j.ijhydene.2017.02.043.

[4] P. González-García, Activated carbon from lignocellulosics precursors: A review of the synthesis methods, characterization techniques and applications, Renew. Sustain. Energy Rev. 82 (August 2017) (2018) 1393–1414, http://dx.doi.org/10.1016/j.rser.2017.04.117.

[5] Z. Zhu, Z. Xu, The rational design of biomass-derived carbon materials towards next-generation energy storage: A review, Renew. Sustain. Energy Rev. 134 (August) (2020) 110308, http://dx.doi.org/10.1016/j.rser.2020.110308.

[6] Z. Roy, S. Barman, G. Halder, Carbon dioxide sorptive cooling in substitute model refrigeration system for replacing halogenated refrigerants, Environ. Technol. Innov. 23 (2021) 101636, http://dx.doi.org/10.1016/j.eti.2021.101636.

[7] A.N. Shafawi, A.R. Mohamed, P. Lahijani, M. Mohammadi, Recent advances in developing engineered biochar for CO2 capture: An insight into the biochar modification approaches, J. Environ. Chem. Eng. 9 (6) (2021) http://dx.doi.org/10.1016/j.jece.2021.106869.

[8] T. Suprianto, Winarto, W. Wijayanti, I.N. Wardana, Synergistic effect of curcumin and activated carbon catalyst enhancing hydrogen production from biomass pyrolysis, Int. J. Hydrogen Energy 46 (10) (2021) 7147–7164, http://dx.doi.org/10.1016/j.ijhydene.2020.11.211.

[9] S. Bennici, P. Dutournié, J. Cathalan, M. Zbair, M.H. Nguyen, E. Scuiller, C. Vaulot, Heat storage: Hydration investigation of MgSO4/active carbon composites, from material development to domestic applications scenarios, Renew. Sustain. Energy Rev. 158 (2022) http://dx.doi.org/10.1016/j.rser.2022.112197.

[10] K. Mitsuoka, S. Hayashi, H. Amano, K. Kayahara, E. Sasaoaka, M.A. Uddin, Gasification of woody biomass char with CO2: The catalytic effects of K and Ca species on char gasification reactivity, Fuel Process. Technol. 92 (1) (2011) 26–31, http://dx.doi.org/10.1016/j.fuproc.2010.08.015.

[11] K. Miura, K. Hashimoto, P.L. Silveston, Factors affecting the reactivity of coal chars during gasification, and indices representing reactivity, Fuel 68 (11) (1989) 1461–1475, http://dx.doi.org/10.1016/0016-2361(89)90046-X.

[12] X. Jing, Z. Wang, Q. Zhang, Z. Yu, C. Li, J. Huang, Y. Fang, Evaluation of CO2 gasification reactivity of different coal rank chars by physicochemical properties, Energy Fuels 27 (12) (2013) 7287–7293, http://dx.doi.org/10.1021/ef401639v.

[13] L. Wang, Ø. Skreiberg, M. Becidan, Investigation of additives for preventing ash fouling and sintering during barley straw combustion, Appl. Therm. Eng. 70 (2) (2014) 1262–1269, http://dx.doi.org/10.1016/j.applthermaleng.2014.05.075.

[14] C. Dupont, S. Jacob, K.O. Marrakchy, C. Hognon, M. Grateau, F. Labalette, D. Da Silva Perez, How inorganic elements of biomass influence char steam gasification kinetics, Energy 109 (2016) 430–435, http://dx.doi.org/10.1016/j.energy.2016.04.094.

[15] Z. Bouraoui, C. Dupont, M. Jeguirim, L. Limousy, R. Gadiou, CO2 gasification of woody biomass chars: The influence of K and Si on char reactivity, Comptes Rendus Chimie 19 (4) (2016) 457–465, http://dx.doi.org/10.1016/j.crci.2015.08.012.

[16] L. Zhang, J. Huang, Y. Fang, Y. Wang, Gasification reactivity and kinetics of typical Chinese anthracite chars with steam and CO2, Energy Fuels 20 (3) (2006) 1201–1210, http://dx.doi.org/10.1021/ef050343o.

[17] B.B. Hattingh, R.C. Everson, H.W. Neomagus, J.R. Bunt, Assessing the catalytic effect of coal ash constituents on the CO2 gasification rate of high ash, South African coal, Fuel Process. Technol. 92 (10) (2011) 2048–2054, http://dx.doi.org/10.1016/j.fuproc.2011.06.003.

[18] P. Sommersacher, T. Brunner, I. Obernberger, Fuel indexes: A novel method for the evaluation of relevant combustion properties of new biomass fuels, Energy Fuels 26 (1) (2012) 380–390, http://dx.doi.org/10.1021/ef201282y.

[19] K. Umeki, A. Moilanen, A. Gómez-Barea, J. Konttinen, A model of biomass char gasification describing the change in catalytic activity of ash, Chem. Eng. J. 207–208 (2012) 616–624, http://dx.doi.org/10.1016/j.cej.2012.07.025.

[20] X. Yao, Q. Yu, Z. Han, H. Xie, W. Duan, Q. Qin, Kinetics of CO2 gasification of biomass char in granulated blast furnace slag, Int. J. Hydrogen Energy 43 (27) (2018) 12002–12012, http://dx.doi.org/10.1016/j.ijhydene.2018.04.102.

[21] E. Mészáros, G. Várhegyi, E. Jakab, B. Marosvölgyi, Thermogravimetric and reaction kinetic analysis of biomass samples from an energy plantation, Energy Fuels 18 (2) (2004) 497–507, http://dx.doi.org/10.1021/ef034030+.

[22] T.G. Bridgeman, L.I. Darvell, J.M. Jones, P.T. Williams, R. Fahmi, A.V. Bridgwater, T. Barraclough, I. Shield, N. Yates, S.C. Thain, I.S. Donnison, Influence of particle size on the analytical and chemical properties of two energy crops, Fuel 86 (1–2) (2007) 60–72, http://dx.doi.org/10.1016/j.fuel.2006.06.022.

[23] T. Mani, P. Murugan, J. Abedi, N. Mahinpey, Pyrolysis of wheat straw in a thermogravimetric analyzer: Effect of particle size and heating rate on devolatilization and estimation of global kinetics, Chem. Eng. Res. Des. 88 (8) (2010) 952–958, http://dx.doi.org/10.1016/j.cherd.2010.02.008.

[24] R. Xiao, W. Yang, X. Cong, K. Dong, J. Xu, D. Wang, X. Yang, Thermogravimetric analysis and reaction kinetics of lignocellulosic biomass pyrolysis, Energy 201 (2020) 117537, http://dx.doi.org/10.1016/j.energy.2020.117537.

[25] A. Gómez-Barea, P. Ollero, C. Fernández-Baco, Diffusional effects in CO2 gasification experiments with single biomass char particles. 1. Experimental investigation, Energy Fuels 20 (5) (2006) 2202–2210, http://dx.doi.org/10.1021/ef050365a.

[26] W. Huo, Z. Zhou, X. Chen, Z. Dai, G. Yu, Study on CO2 gasification reactivity and physical characteristics of biomass, petroleum coke and coal chars, Bioresour. Technol. 159 (2014) 143–149, http://dx.doi.org/10.1016/j.biortech.2014.02.117.

[27] S.S. Vincent, N. Mahinpey, A. Aqsha, Mass transfer studies during CO2 gasification of torrefied and pyrolyzed chars, Energy 67 (2014) 319–327, http://dx.doi.org/10.1016/j.energy.2013.12.034.

[28] T. Mani, N. Mahinpey, P. Murugan, Reaction kinetics and mass transfer studies of biomass char gasification with CO2, Chem. Eng. Sci. 66 (1) (2011) 36–41, http://dx.doi.org/10.1016/j.ces.2010.09.033.

[29] R. Xiao, W. Yang, Kinetics characteristics of straw semi-char gasification with carbon dioxide, Bioresour. Technol. 207 (2016) 180–187, http://dx.doi.org/10.1016/j.biortech.2016.02.010.

[30] Y.T. Kim, D.K. Seo, J. Hwang, Study of the effect of coal type and particle size on char-CO2 gasification via gas analysis, Energy Fuels 25 (11) (2011) 5044–5054, http://dx.doi.org/10.1021/ef200745x.

[31] G. Wang, J. Zhang, X. Hou, J. Shao, W. Geng, Study on CO2 gasification properties and kinetics of biomass chars and anthracite char, Bioresour. Technol. 177 (2015) 66–73, http://dx.doi.org/10.1016/j.biortech.2014.11.063.

[32] S. Li, H. Song, J. Hu, H. Yang, J. Zou, Y. Zhu, Z. Tang, H. Chen, CO2 gasification of straw biomass and its correlation with the feedstock characteristics, Fuel 297 (March) (2021) 120780, http://dx.doi.org/10.1016/j.fuel.2021.120780.

[33] FAOSTAT, Food and Agriculture Organization of the United Nations, 2023, https://www.fao.org/faostat/en/#data/QCL. (Last Accessed 31 January 2023).

[34] A. González-Cencerrado, J. Pallarés, M.T. López-Franco , B. Rebolledo, Assessing the environmental benefit of a new fertilizer based on activated biochar applied to cereal crops, Sci. Total Environ. 711 (2020) 134668, http://dx.doi.org/10.1016/j.scitotenv.2019.134668.

[35] M. Gil, I. Arauzo, Hammer mill operating and biomass physical conditions effects on particle size distribution of solid pulverized biofuels, Fuel Process. Technol. 127 (2014) 80–87, http://dx.doi.org/10.1016/j.fuproc.2014.06.016.

[36] P. Adapa, L. Tabil, G. Schoenau, Compaction characteristics of barley, canola, oat and wheat straw, Biosyst. Eng. 104 (3) (2009) 335–344, http://dx.doi.org/10.1016/j.biosystemseng.2009.06.022.

[37] J.R. Hess, D.N. Thompson, R.L. Hoskinson, P.G. Shaw, D.R. Grant, Physical separation of straw stem components to reduce silica, Appl. Biochem. Biotechnol. 2003 105:1 105 (1) (2003) 43–51, http://dx.doi.org/10.1385/ABAB:105:1-3:43.
[38] W. Wu, Y. Mei, L. Zhang, R. Liu, J. Cai, Kinetics and reaction chemistry of pyrolysis and combustion of tobacco waste, Fuel 156 (2015) 71–80, http://dx.doi.org/10.1016/j.fuel.2015.04.016.
[39] J. Cai, D. Xu, Z. Dong, X. Yu, Y. Yang, S.W. Banks, A.V. Bridgwater, Processing thermogravimetric analysis data for isoconversional kinetic analysis of lignocellulosic biomass pyrolysis: Case study of corn stalk, Renew. Sustain. Energy Rev. 82 (April 2017) (2018) 2705–2715, http://dx.doi.org/10.1016/j.rser.2017.09.113.
[40] W. Tong, Q. Liu, C. Yang, Z. Cai, H. Wu, S. Ren, Effect of pore structure on CO2 gasification reactivity of biomass chars under high-temperature pyrolysis, J. Energy Inst. 93 (3) (2020) 962–976, http://dx.doi.org/10.1016/j.joei.2019.08.007.
[41] H. Tian, Y. Wei, S. Cheng, Z. Huang, M. Qing, Y. Chen, H. Yang, Y. Yang, Optimizing the gasification reactivity of biochar: The composition, structure and kinetics of biochar derived from biomass lignocellulosic components and their interactions during gasification process, Fuel 324 (PC) (2022) 124709, http://dx.doi.org/10.1016/j.fuel.2022.124709.
[42] C. Serrano, E. Monedero, M. Lapuerta, H. Portero, Effect of moisture content, particle size and pine addition on quality parameters of barley straw pellets, Fuel Process. Technol. 92 (3) (2011) 699–706, http://dx.doi.org/10.1016/j.fuproc.2010.11.031.
[43] F. Sher, S.Z. Iqbal, H. Liu, M. Imran, C.E. Snape, Thermal and kinetic analysis of diverse biomass fuels under different reaction environment: A way forward to renewable energy sources, Energy Convers. Manage. 203 (September 2019) (2020) 112266, http://dx.doi.org/10.1016/j.enconman.2019.112266.
[44] J. Pallarés, A. González-Cencerrado, I. Arauzo, Production and characterization of activated carbon from barley straw by physical activation with carbon dioxide and steam, Biomass Bioenergy 115 (January) (2018) 64–73, http://dx.doi.org/10.1016/j.biombioe.2018.04.015.
[45] B.M. Jenkins, L.L. Baxter, T.R. Miles, T.R. Miles, Combustion properties of biomass, Fuel Process. Technol. 54 (1–3) (1998) 17–46, http://dx.doi.org/10.1016/S0378-3820(97)00059-3.
[46] S.V. Vassilev, D. Baxter, L.K. Andersen, C.G. Vassileva, An overview of the chemical composition of biomass, Fuel 89 (5) (2010) 913–933, http://dx.doi.org/10.1016/j.fuel.2009.10.022.
[47] S. Naik, V.V. Goud, P.K. Rout, K. Jacobson, A.K. Dalai, Characterization of Canadian biomass for alternative renewable biofuel, Renew. Energy 35 (8) (2010) 1624–1631, http://dx.doi.org/10.1016/j.renene.2009.08.033.
[48] T. Qu, X. Zhang, X. Gu, L. Han, G. Ji, X. Chen, W. Xiao, Ball milling for biomass fractionation and pretreatment with aqueous hydroxide solutions, ACS Sustain. Chem. Eng. 5 (9) (2017) 7733–7742, http://dx.doi.org/10.1021/acssuschemeng.7b01186.
[49] C. Di Blasi, Combustion and gasification rates of lignocellulosic chars, Prog. Energy Combust. Sci. 35 (2) (2009) 121–140, http://dx.doi.org/10.1016/j.pecs.2008.08.001.
[50] M. Müller-Hagedorn, H. Bockhorn, Pyrolytic behaviour of different biomasses (angiosperms) (maize plants, straws, and wood) in low temperature pyrolysis, J. Anal. Appl. Pyrolysis 79 (1-2 SPEC. ISS) (2007) 136–146, http://dx.doi.org/10.1016/j.jaap.2006.12.008.
[51] J.A. Caballero, J.A. Conesa, R. Font, A. Marcilla, Pyrolysis kinetics of almond shells and olive stones considering their organic fractions, J. Anal. Appl. Pyrolysis 42 (2) (1997) 159–175, http://dx.doi.org/10.1016/S0165-2370(97)00015-6.
[52] B. Janković, N. Manić, D. Stojiljković, V. Jovanović, TSA-MS characterization and kinetic study of the pyrolysis process of various types of biomass based on the Gaussian multi-peak fitting and peak-to-peak approaches, Fuel 234 (July) (2018) 447–463, http://dx.doi.org/10.1016/j.fuel.2018.07.051.
[53] F. Cheng, H. Bayat, U. Jena, C.E. Brewer, Impact of feedstock composition on pyrolysis of low-cost, protein- and lignin-rich biomass: A review, J. Anal. Appl. Pyrolysis 147 (August 2019) (2020) 104780, http://dx.doi.org/10.1016/j.jaap.2020.104780.
[54] P.R. Patwardhan, J.A. Satrio, R.C. Brown, B.H. Shanks, Influence of inorganic salts on the primary pyrolysis products of cellulose, Bioresour. Technol. 101 (12) (2010) 4646–4655, http://dx.doi.org/10.1016/j.biortech.2010.01.112.
[55] M.E. Fuentes, D.J. Nowakowski, M.L. Kubacki, J.M. Cove, T.G. Bridgeman, J.M. Jones, Survey of influence of biomass mineral matter in thermochemical conversion of short rotation willow coppice, J. Energy Inst. 81 (4) (2008) 234–241, http://dx.doi.org/10.1179/014426008X370942.
[56] J. Alvarez, G. Lopez, M. Amutio, J. Bilbao, M. Olazar, Kinetic study of carbon dioxide gasification of rice husk fast pyrolysis char, Energy Fuels 29 (5) (2015) 3198–3207, http://dx.doi.org/10.1021/acs.energyfuels.5b00318.
[57] X. Zeng, K. Kahara, Y. Ueki, R. Yoshiie, G. Xu, I. Naruse, Characteristics of biomass devolatilization and in Situ Char gasification tested by the non-isothermal method, Energy Fuels 33 (10) (2019) 9805–9817, http://dx.doi.org/10.1021/acs.energyfuels.9b00672.
[58] H. Tian, Q. Hu, J. Wang, D. Chen, Y. Yang, A.V. Bridgwater, Kinetic study on the CO2 gasification of biochar derived from Miscanthus at different processing conditions, Energy 217 (2021) 119341, http://dx.doi.org/10.1016/j.energy.2020.119341.
[59] Y. Zhao, D. Feng, Y. Zhang, Y. Huang, S. Sun, Effect of pyrolysis temperature on char structure and chemical speciation of alkali and alkaline earth metallic species in biochar, Fuel Process. Technol. 141 (2016) 54–60, http://dx.doi.org/10.1016/j.fuproc.2015.06.029.
[60] N. Halim, A. Tajima, S. Asano, S. Kudo, J.I. Hayashi, Change in catalytic activity of potassium during CO2 gasification of char, Energy Fuels 34 (1) (2020) 225–234, http://dx.doi.org/10.1021/acs.energyfuels.9b03630.
[61] A. Bach-Oller, E. Furusjö, K. Umeki, On the role of potassium as a tar and soot inhibitor in biomass gasification, Appl. Energy 254 (May) (2019) http://dx.doi.org/10.1016/j.apenergy.2019.113488.
[62] W. Liang, X. Ning, G. Wang, J. Zhang, R. Li, W. Chang, C. Wang, Influence mechanism and kinetic analysis of co-gasification of biomass char and semi-coke, Renew. Energy 163 (2021) 331–341, http://dx.doi.org/10.1016/j.renene.2020.08.142.
[63] K. Xu, S. Hu, S. Su, C. Xu, L. Sun, C. Shuai, L. Jiang, J. Xiang, Study on char surface active sites and their relationship to gasification reactivity, Energy Fuels 27 (1) (2013) 118–125, http://dx.doi.org/10.1021/ef301455x.